RIO

PUC

Dissertação de Mestrado

A reduced order model for unsteady state of a laminar separation bubble using experimental data

João Victor Neves Neiva

Pontifícia Universidade Católica do Rio de Janeiro
Centro Técnico Científico
Departamento de Engenharia Mecânica

Rio de Janeiro, 17 de dezembro de 2025

Pontifícia
Universidade
Católica do
Rio de Janeiro

A reduced order model for unsteady state of a laminar separation bubble using experimental data

João Victor Neves Neiva

Orientação: Professor Igor Braga de Paula
Coorientação: Professor Luc Pastur

Dissertação apresentada como requisito parcial para a obtenção do grau de Mestre em Engenharia Mecânica pelo programa de Pós-Graduação em Engenharia Mecânica no Departamento Engenharia Mecânica

Rio de Janeiro, 17 de dezembro de 2025

Pontifícia
Universidade
Católica do
Rio de Janeiro

A Reduced order model for unsteady state of a laminar separation bubble using experimental data

João Victor Neves Neiva

Dissertação apresentada como requisito parcial para a obtenção do grau de Mestre em Engenharia Mecânica Aprovada pela Comissão examinadora abaixo:

Professor Igor Braga de Paula
Orientador
Departamento de Engenharia Mecânica – PUC-Rio

Professor Luc Pastur
Co-orientador
IP-Paris/ENSTA

Professor André Valdetaro Gomes Cavalieri
ITA-São José dos Campos

Professor Fábio Jessen Werneck de Almeida Martins
Departamento de Engenharia Mecânica – PUC-Rio

Rio de Janeiro, 17 de dezembro de 2025

Pontifícia
Universidade
Católica do
Rio de Janeiro

João Victor Neves Neiva
Graduou-se em engenharia mecânica na Pontifícia Universidade Católica do Rio de Janeiro em dezembro de 2023. Trabalha no Laboratory of Mechanics and Interfaces (LMI) na ENSTA – Institute Polytechnique de Paris, com foco em modelos de ordem reduzida e sistemas dinâmicos.

Bibliographic data

Neiva, João Victor Neves

A reduced order model for the unsteady state of a laminar separation bubble using experimental data / João Victor Neves Neiva ; orientador: Igor B. de Paula ; co-orientador: Luc Pastur. – 2025.
89 f. : il. color. ; 30 cm

Dissertação (mestrado)–Pontifícia Universidade Católica do Rio de Janeiro, Departamento de Engenharia Mecânica, 2025.
Inclui bibliografia

1. Engenharia Mecânica – Teses. 2. Bolha de separação laminar. 3. Modelo de ordem reduzida. 4. Dados experimentais. 5. Mecânica dos fluidos. 6. Identificação de sistemas. I. Paula, Igor Braga de. II. Pastur, Luc. III. Pontifícia Universidade Católica do Rio de Janeiro. Departamento de Engenharia Mecânica. IV. Título.

CDD: 621

To my family.

Acknowledgments

The list of people I would like to thank for their support over the past two years is much longer than can be written here.

Without the full dedication and support of my mother, Eliane, and my grandmother, Marília, it would have been impossible for me to become who I am today. Thank you both for everything you have done for me throughout my life. Without your sacrifices, I would never have made it this far. I would also like to thank my sister for everything we share. Thank you for showing me a new perspective every day. And thank you to my family, who I praise the most.

I would like to thank also my colleagues and friends, Dehui, Francisco and Mathias. Without you, those years would have been tougher. You certainly made them easier. Also, I would like to thank my dear friend Alexandre who has always been there for me. Thank you for your friendship no matter when or where.

I would like to express my gratitude to Professor Dr. Daniel Rodríguez Álvarez who has always been willing to help when needed. Thank you for always taking the discussion further.

This research would not have been possible without the dedication and collaboration of three exceptional individuals, whom I can't thank enough: Omar Pinedo, Professor Igor B. de Paula and Professor Luc Pastur.

Without Omar's excellent research, we would not have achieved our result. Furthermore, without the meetings and your support, we would not have succeeded. Thank you very much.

Professor Igor, thank you for making this year easier. I still don't know how you agreed to take on a Master's student who was moving to another country and needed to find a research proposal. I admire your knowledge and your approach to problem-solving. Thank you for being such a great advisor and role model throughout this year.

Professor Luc, thank you for welcoming me to France so warmly just after I arrived. Your knowledge, your field of study, your approach to problems and your kindness make you a role model for me. I could never thank you enough for all the opportunities you have given me.

My wife, Olivia, who is the foundation of my everyday life. You are my inspiration. Thank you for reminding me every day that kindness is not a weakness, but the strongest of all characteristics. Without you, we would never have achieved this. You are an important part of this work.

This study was financed in part by the *Coordernação de Aperfeiçoamento de Pessoal do Nível Superior*-Brasil (CAPES) - Finance Code 001

Abstract

Neves Neiva, João Victor; Braga de Paula, Igor (Advisor); Pastur, Luc (Co-Advisor). **A reduced order model for unsteady state of a laminar separation bubble using experimental data**. Rio de Janeiro, 2025. 89p. Dissertação de Mestrado – Departamento de Engenharia Mecânica, Pontifícia Universidade Católica do Rio de Janeiro.

Laminar separation bubbles (LSBs) have a significant role in the aerodynamic performance of airfoils operating at low Reynolds numbers. In many applications, they are subject to a time-varying level of environmental disturbances, such as in turbine cascades and unmanned aerial vehicles. This time–varying regime is not yet fully described. In this scenario, reduced order models emerge as useful tool to help describing and modeling the phenomenon. In this work, a four-dimensional and a three dimensional Galerkin model using Proper Orthogonal Decompostion (POD) and Sparse Identification of Dynamical System (SINDy) are tested for modeling the formation of a LSB. The model is built using experimental data from time-resolved Particle Image Velocimetry measurements of a flow over a flat plate in a water tunnel with a convergent divergent geometry. To this end, the vorticity transport formulation of the incompressible Navier-Stokes equation is used to identify the steady solutions. Two flow states are identified and used as flow fields for the modal decomposition, and therefore, for the models. The first modal decomposition has four most energetic modes, according to POD. Two static modes (u1 and u2) and two oscillatory modes (u3 and u4). The time dynamics of the third and fourth modes indicate an oscillating permanent regime reached after a transient. The resulting four-dimensional POD-Galerkin model correctly predicts the full transient dynamics, from the beginning of the boundary layer separation until the permanent regime with vortex shedding. The second modal decomposition has three most energetic modes and is in accordance with literature. The first mode is a static mode (u3), known as shift mode, and two oscillatory modes (u1, u2). The model retrieves the famous Landau equation and conjecture a Hopf bifurcation as the route for the dynamical system. Although the model only captures the transient part just before the boundary layer transition, it correctly predicts the dynamics.

Keywords

Reduced order model; POD; SINDy; Laminar separation bubble; Fluid mechanics.

Resumo

Neves Neiva, João Victor; Braga de Paula, Igor; Pastur, Luc. **Modelo de ordem reduzida para o estado transiente da bolha de separação laminar usando dados experimentais**. Rio de Janeiro, 2025. 89p. Dissertação de Mestrado – Departamento de Engenharia Mecânica, Pontifícia Universidade Católica do Rio de Janeiro.

As bolhas de separação laminar (LSBs) desempenham um papel significativo na performance aerodinâmica de aerofólios que operam em números de Reynolds baixos. Em muitas aplicações, elas estão sujeitas a distúrbios ambientais que variam no tempo, como em turbinas e veículos aéreos não tripulados. Esse regime de variação temporal ainda não está totalmente descrito. Nesse cenário, os modelos de ordem reduzida surgem como uma ferramenta útil para auxiliar na descrição e modelagem do fenômeno. Neste trabalho, um modelo de Galerkin quadridimensional e um tridimensional, utilizando Decomposição Ortogonal Própria (POD) e Identificação Esparsa de Sistemas Dinâmicos (SINDy), são testados para modelar a formação de uma LSB. O modelo é construído usando dados experimentais de medições de velocimetria por imagem de partículas resolvida no tempo de um escoamento sobre uma placa plana em um túnel de água com geometria convergente-divergente. Para isso, a formulação de transporte de vorticidade da equação de Navier-Stokes incompressível é utilizada para identificar as soluções estacionárias. Dois estados são identificados e usados como campos de escoamento para a decomposição modal e, portanto, para os modelos. A primeira decomposição modal possui quatro modos mais energéticos, de acordo com a POD: dois modos estáticos (u1 e u2) e dois modos oscilatórios (u3 e u4). A dinâmica temporal do terceiro e quarto modos indica um regime permanente oscilatório alcançado após um transiente. O modelo POD-Galerkin quadridimensional resultante prevê corretamente toda a dinâmica transiente, desde o início da separação da camada limite até o regime permanente com o desprendimento de vórtices. A segunda decomposição modal possui os três modos mais energéticos e está em conformidade com a literatura. O primeiro modo é um modo estático (u1), conhecido como modo de deslocamento (shift mode), e dois modos oscilatórios (u2,u3). O modelo recupera a famosa equação de Landau e conjectura uma bifurcação de Hopf como a rota para o sistema dinâmico. Embora o modelo capture apenas a parte transiente logo antes da transição da camada limite, ele prevê corretamente a dinâmica.

Palavras-chave

Modelo de ordem reduzida; POD; SINDy; Bolha de separação laminar; Mecânica dos fluidos.

Table of contents

List of figures

List of tables

List of Abreviations

UAV(s) – unmanned aerial vehicle(s)

MAV(s) – micro aerial vehicle(s)

Re – Reynolds number

LSB(s) – laminar separation bubble(s)

ROM(s) – reduced order model(s)

CFD – computational fluid dynamics

POD – proper orthogonal decomposition

PIV – Particle Image Velocimetry

K-H – Kelvin Helmholtz

T-S – Tollmien-Schlichting

DNS – direct numerical simulation

PCA – Principal Component Analysis

N-S – Navier-Stokes

ODE(s) – ordinary differential equation(s)

SINDy – Sparse Identification of Nonlinear Dynamics

URANS – Unsteady Reynolds-Averaged Navier-Stokes

SR-3 – Sparse Relaxed Regularized Regression

SVD – Single Value Decomposition

PySINDy – Python Sparse Identification of Nonlinear Dynamics

Bear and face all calamities and adversities
with patience and pure conscience;

Inazo Nitobe, *Bushido the Soul of Japan.*

1
Introduction

The relevance of laminar separation bubbles to engineering applications is briefly discussed in this introduction to present a motivation for the study. For contextualization, the chapter also includes a general description of the phenomena and the importance of reduced-order models for predicting the bubble behavior. At the end of the chapter, the dissertation objectives are outlined.

1.1
Contextualization and research motivation

Within the framework of globalization, there is a growing demand for technologies to reduce transportation and energy generation costs. Investments in new designs of low-pressure turbines, wind turbines, unmanned aerial vehicles (UAVs), and micro aerial vehicles (MAVs) are therefore of strategic importance. In these applications, the Reynolds number, defined as $Re = \frac{U\,c}{\nu}$, where U denotes the free-stream velocity, c the airfoil chord length, and ν the kinematic viscosity, generally lies within the range 10^4–10^6 [30]. Under low Re conditions, the laminar boundary layer over the airfoils is long, and in the presence of an adverse pressure gradient, it may separate on its suction side. The separated flow can transition from laminar to turbulent, leading to subsequent reattachment and, hence, giving rise to a laminar separation bubble (LSB) [3]. Systems operating at low Reynolds numbers and subject to high aerodynamic loading typically exhibit this phenomenon [29, 15]. This flow configuration is of fundamental interest from a fluid-mechanical point of view and of considerable technological relevance [1].

The presence of a LSB can modify the global pressure distribution over the airfoil and degrade aerodynamic performance [1]. In addition, Gaster (1967) and Horton (1968) [1, 2] demonstrated that, at low Mach numbers, airfoil stall is strongly influenced by the dynamics of small bubbles formed on the airfoil leading edge at incidence angles below those of maximum lift. The dynamics of LSB are also very relevant for noise emission and structure vibration [4]. Consequently, LSBs may be typically regarded as parasitic flow features in airfoils [4].

The work of Gaster (1967) [1] showed that LSBs are highly sensitive to environmental disturbances, which can substantially alter their structure and dynamics. The majority of existing investigations on laminar separation bubbles have focused on the quasi-steady flow regime. This corresponds to a regime of constant environmental conditions. However, variations in background disturbance levels are a typical scenario in rotating blades, turbine cascades, and many other systems. Conversely, the regime of varying environmental disturbances has received comparatively little attention in the literature [21]. The aerodynamic performance of airfoils in this regime can be significantly different (e.g., Mayle (1991) [66]). This can change stall, drag, and acoustic emissions. The relatively low number of works devoted to this topic may be attributed to challenges for experiments and simulations. From the experimental perspective, it demands high temporal and spatial resolution and advanced control of environmental disturbances. Marxen and Henningson (2011) [51] demonstrated that accurately capturing the dynamics of LSBs via numerical simulations requires substantial computational resources. This is still valid nowadays. Therefore, there remains a need for modeling strategies capable of reliably predicting LSB dynamics, particularly in transient regimes [17].

Driven by rapid advances in data science technology, data-driven modeling methodologies have gained substantial prominence. They are now widely employed in serveral research areas, including fluid dynamics. The simulation of many fluid-dynamical problems demands accurate, high-fidelity numerical solutions of the Navier–Stokes equations, which are typically costly. Also, experiments under strictly controlled conditions can be difficult to implement and are often expensive. Thus, their systematic use in engineering applications is usually impractical [26]. These limitations have motivated the development of reduced-order models (ROMs) [37].

As discussed in Noack et al. [33], the identification of suitable actuation and sensing strategies, as well as the design of effective control laws, is expensive using conventional computational fluid dynamics (CFD) frameworks. This cost motivates the development of low-dimensional flow representations for engineering applications. Furthermore, as emphasized in Noack et al. [32], such reduced-order descriptions offer an interesting framework for elucidating dominant physical mechanisms, conducting rapid parametric or exploratory studies of actuation concepts, and systematically exploiting tools from control theory and dynamical systems. Consequently, coherent-structure-based models help narrow the conceptual and practical gap between analytical approaches and fully resolved, high-dimensional simulations.

As noted by Almutairi et al. [7], the incomplete understanding of the

underlying separation-bubble physics continues to hinder the design and implementation of effective flow-control strategies intended to mitigate their detrimental effects. Owing to the intrinsic complexity of the phenomenon, no existing model currently provides a robust prediction of the flow response across a broad range of operating conditions.

This study aims to develop and evaluate a reduced-order model describing the transient growth of a laminar separation bubble. The configuration under consideration corresponds to a bubble subjected to pronounced, rapid variations in the background disturbance level. The reduced-order model is further used to elucidate the underlying physical mechanisms governing the formation, development, and evolution of the recirculating bubble.

1.2 Objectives and outline

The objective of this work is to develop and assess a reduced-order model capable of describing the asymptotic growth of a laminar separation bubble, using the experimental dataset provided by Horna (2024) [63].

The structure of this thesis is as follows. Chapter 1 introduces the research topic and delineates the motivation and context of the present study. Chapter 2 presents a comprehensive review of the relevant literature and fundamental concepts underlying the problem. Chapter 3 examines the experimental work of Horna [63], and introduces the mathematical foundations that support the theoretical framework of the reduced-order model. Chapter 4 presents and critically analyzes the results, including an in-depth discussion of their physical and methodological implications. Finally, Chapter 5 synthesizes the main conclusions and outlines potential avenues for future research.

2
Literature Review

This chapter presents a literature survey of topics relevant to this work, including laminar separation bubbles and reduced-order models, specifically the POD-Galerkin projection technique.

2.1
Laminar separation bubble

In the actual context of the global economy and the environment, new technologies are required to reduce transportation costs, noise, and emissions [71]. Therefore, there is an intense effort to improve the performance of all kinds of vehicles. Many of these vehicles have important elements that operate at low Reynolds-number regimes, such as turbines in aircraft, wings and propellers in unmanned aerial vehicles and micro aerial vehicles and many others. Conditions of Re within the range $10^4 - 10^6$ is sufficiently low that the viscous boundary layer rarely remains attached in the whole extent of high lift airfoils [30]. The combination of low Reynolds numbers and high aerodynamic loads in airfoils usually imposes strong adverse pressure gradients on the laminar boundary layers, hence promoting flow deattachment [29, 15]. In this case, the shear layer of the separated flow can exhibit a transition to turbulence. The turbulence may induce a flow reattachment, thus forming a laminar separation bubble [3] (Figure 2.1). This is a relevant phenomenon in aerodynamics that influences many practical applications [10].

The LSB modifies the pressure distribution over airfoils (Figure 2.2), thereby influencing their performance. For instance, LSB can promote stall, high drag, high vibration, and high aeroacoustic noise [1, 2, 29, 47, 12]. According to Almutairi et al. [7], the occurrence of an LSB can also produce undesirable phenomena, including flow oscillations driven by bubble flapping and abrupt stall of the airfoil caused by bubble breakdown. As noted in the works of Gaster (1967) and Horton (1968) [1, 2], the stall characteristics of airfoils at low subsonic speeds are closely related to the behavior of small bubbles near the leading edge at incidence angles lower than those corresponding

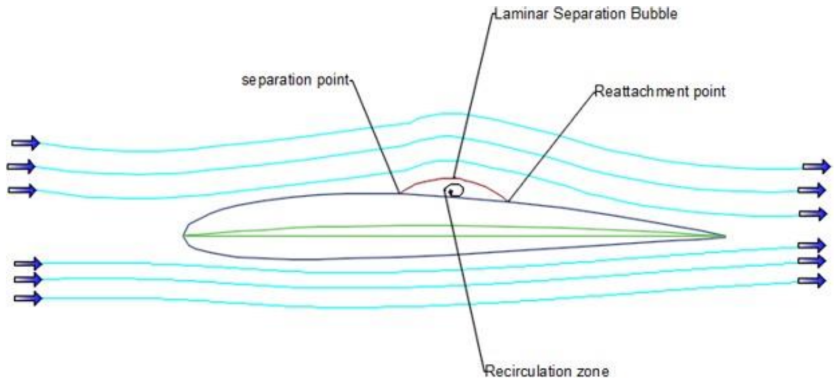

Figure 2.1: Scheme of a laminar separation bubble on an airfoil. Extracted from Thompson and Gunasekaran [4]

.

to maximum lift. Furthermore, Michelis et al. [19], highlights that an LSB is highly sensitive to environmental disturbances, which can significantly modify its properties (Figure: 2.6).

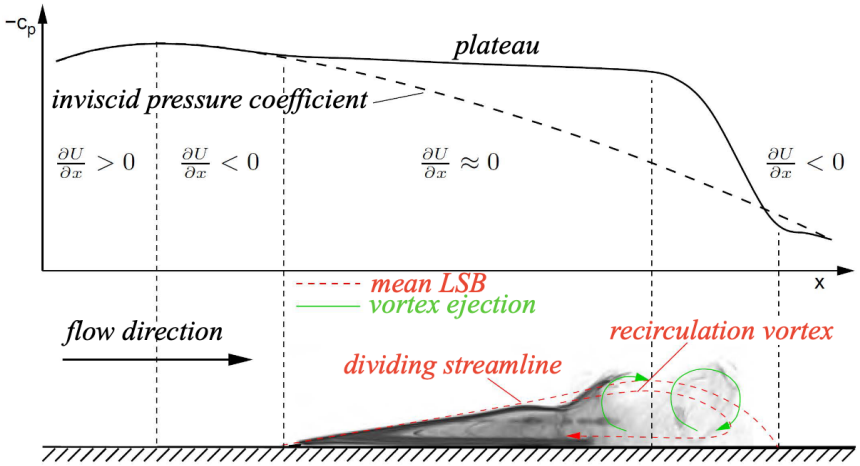

Figure 2.2: Schematic representation of the influence of a laminar separation bubble on the pressure coefficient Lang et al. (2004) [65]. Adapted by Horna (2024) [63]

.

According to this brief introduction, one can note that LSB characteristics depend on flow conditions and can significantly affect aerodynamic devices [4]. Therefore, some relevant bubble characteristics for this work are briefly described in the next section.

2.1.1 Characteristics of Laminar Separation Bubbles

The contributions from the works of Gaster (1967) and Horton (1968) [1, 2] revealed many features of laminar separation bubbles. According to their description, the bubble initiates at a stagnation point, where the flow first detaches from the surface until its reattachment further downstream. Between the separation and reattachment locations, the flow can be separated into two principal regions. The first is the free shear layer, which lies between the outer edge of the viscous region and the dividing streamline (see Figure 2.3). The second is the recirculation bubble, bounded by the mean dividing streamline and the wall. Each of these regions can, in turn, be split into portions upstream and downstream of the transition point (denoted by T^* in the Figure 2.3), which is near the maximum height point. Upstream of the transition location, the momentum near the wall is lower than in turbulent flows, and the boundary layer is therefore more prone to separation under the influence of adverse pressure gradients. Once transition to turbulence occurs, the effective mean shear stress in the layer increases by at least an order of magnitude, allowing the pressure to rise until reattachment occurs at a value close to that of the inviscid outer flow [2]. Equivalently, one may state that turbulent entrainment energizes the shear layer, enabling this pressure recovery. In the vicinity of reattachment, there is a quasi-periodic shedding of spanwise roll-up vortices [72]. Figure 2.3 summarizes this description, presenting a schematic of the main topological features of an LSB. In a time-averaged sense, the LSB is enclosed by a streamline that defines a closed region with zero net mass flow [2].

According to Diwan and Ramesh (2007) [3] if the boundary layer stays laminar up to the separation point, the shear layer immediately downstream of this point will also be laminar and intrinsically unstable. Consequently, energy is transferred from the mean shear flow into unstable disturbances, promoting growth as they propagate downstream. This process can ultimately initiate the transition from laminar to turbulent flow. In the initial part of an LSB, commonly referred to as the dead-air region, the flow is essentially steady, and the magnitude of the reverse flow is relatively small [2]. In contrast, near the turbulent portion of the bubble, reverse flow levels are high, and the flow becomes strongly unsteady due to the quasi-periodic shedding of spanwise roll-up vortices. These spanwise vortices quickly break down into turbulence near the reattachment location under the influence of various instability mechanisms, e.g., global instabilities [70], secondary instabilities [52], or the

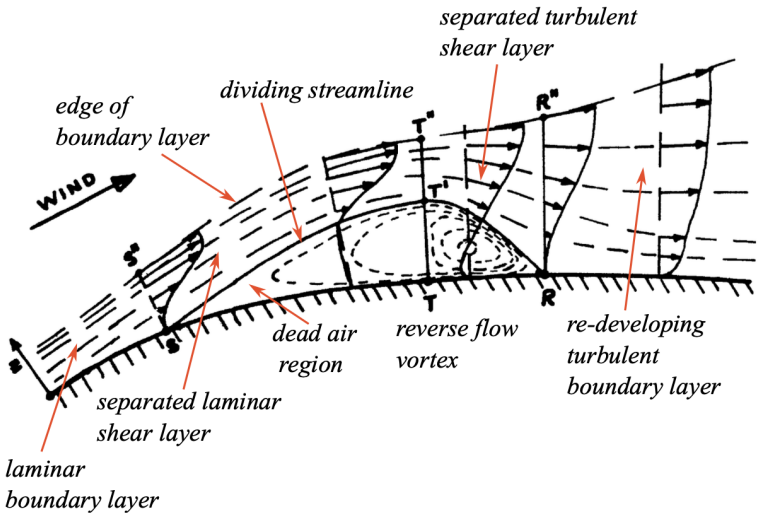

Figure 2.3: Scheme of an LSB on an airfoil. **S** is the separation point, **T** is the transition point, and **R** is the reattachment point of the boundary layer. The separated shear layer region is delimited by **S-S"-R"-R**. The laminar separation bubble is delimited by **S-T'-R**. Image extracted from Horton (1968) [2], and adapted by Horna (2024) [63]

.

superposition of oblique disturbance waves [20]. Thus, the reattachment region itself is marked by pronounced nonlinear dynamics and instabilities [3].

Accordingly to Lengani et al. (2017) [8], near the separation point the velocity fluctuations within the bubble may undergo exponential growth, causing the shear layer to roll up beyond the location of maximum bubble heigh. The author also notes that large-scale coherent structures promote both the transition of the separated shear layer and its subsequent reattachment. It was also observed that near the separation point, turbulent kinetic energy is predominantly generated by low-frequency velocity oscillations. In this, the production of stresses is mostly governed by the normal straining of the fluid elements. Conversely, near the reattachment, turbulence production is almost entirely attributed to shear.

In the context of LSBs, the terms *flapping* and *breathing* are frequently related to low-frequency vertical oscillation or wavering of the shear layer and to low-frequency streamwise variations of the reattachment point [31]. In this case, the LSB undergoes alternating phases of expansion and contraction, predominantly in its aft region. As Malmir et al. (2024) [31], points out, the term *breathing* is now more commonly employed than *flapping*. Simoni et al. (2012) [69], demonstrated that bubble flapping is sensitive to incoming flow

disturbances. Despite extensive observations of this low-frequency behavior, its role in the bubble dynamics is not yet fully understood. The current work aims to shed further light on this topic. Indeed, according to Dovgal et al. (1994) [10], the unsteady behavior of separated boundary-layer flows is a multifaceted issue and it still demands clarification.

The LSB is commonly categorized as either short or long, although there is no entirely consistent definition in the literature. Figure 2.4 shows the contrast in pressure coefficient between short (left) and long (right) bubbles. Serna and Lázaro (2015) [17], provides an overview of the different perspectives on the topic. Tani (1964) [48], argued that long bubbles exert a global influence on the pressure distribution over the airfoil surface, whereas the impact of short bubbles is restricted to a more localized region. Gaster (1967) [1], reported for short bubbles that time-averaged flow in the reattachment region is dominated by a vortex-like structure whose characteristic size is comparable to the height of the recirculation zone. According to Thompson and Gunasekaran (2021) [4], a short bubble is always confined between the separation and reattachment points, whereas, in the case of a long bubble, the separated flow may reattach at the trailing edge (see Figure 2.4). Furthermore, its occurrence is restricted to a certain Reynolds-number range that depends on the surface pressure distribution, the airfoil geometry, surface irregularities, and the free-stream turbulence level. As noted by Serna and Lázaro (2015) [17], the formulation of a universal criterion to predict the occurrence of long or short bubbles is challenging, given the wide variety of laminar separation configurations. Indeed, many aspects of long and short bubbles make it difficult to establish robust criteria for describing their behavior.

According to Serna and Lázaro (2015) [17], an important feature associated with LSBs is the occurrence, under certain flow conditions, of so-called *bubble bursting* events, which involve a rapid transition between short- and long-bubble states. These events can be understood as a temporary failure of the turbulent shear-layer reattachment process, and they attract attention because of their connection to stall behavior [17]. Gaster (1967) [1] suggested a feedback mechanism in an attempt to explain *bursting*, such that as the free stream velocity is decreased the upstream perturbation of the pressure distribution, caused by the presence of the bubble, increases as the bubble expands in such a way as to decrease the boundary layer Reynolds number at separation, leading to a further increase in bubble size, and so on until bursting occurs.

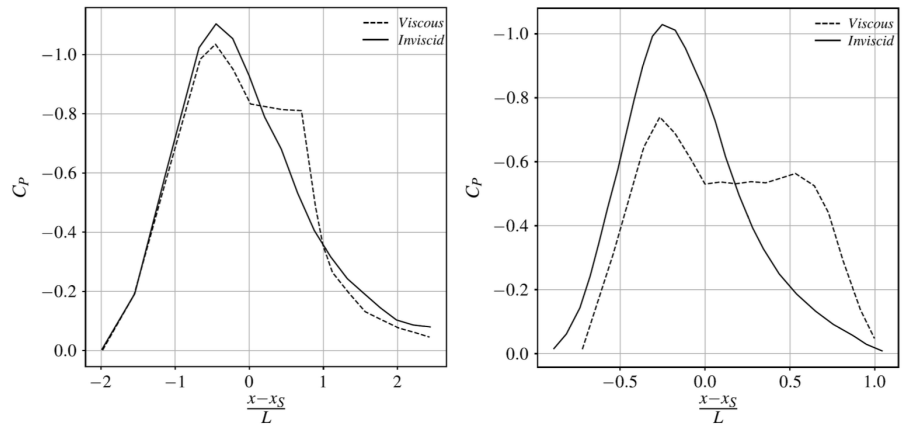

Figure 2.4: Pressure coefficient of a short LSB (left) and a long LSB (right). The data was measured by Gaster (1967) [1]. Image extracted from Mitra and Ramesh (2019) [67]

Gaster (1967) [1], conducted an experimental investigation of the LSB over a broad range of Reynolds numbers and under various pressure distributions, employing hot-wire measurements to obtain the data. The aim was to establish a criterion for bubble bursting. The findings indicated that the bubble's structure is governed by the separation Reynolds number $Re_s = \frac{U_s \theta_s}{\mu}$ and the momentum thickness at separation, $\theta_s = \int_0^\infty \frac{u}{U_\infty}(1 - \frac{u}{U_\infty})dy$. Gaster (1967), [1], suggest building a relation between Re_s and a parameter characterizing the mean velocity gradient along the bubble length to establish a criterion for bubble bursting.

Horton (1968) [2], also investigated the conditions under which bursting can be initiated. He conducted experiments to characterize the growth and bursting behavior of short bubbles and introduced a new criterion for identifying reattachment. Later, Serna and Lázaro (2015) [17], revisited the problem and proposed an alternative bursting criterion based on the topology of vortex blobs generated during the transition process. Their findings were based on Particle Image Velocimetry measurements of separated flow over a flat plate subjected to an imposed adverse pressure gradient. Within a particular parametric space, they found a narrow range of critical Reynolds numbers that separates two distinct reattachment regimes. For Reynolds numbers within this range, the reattachment does occur shortly after transition onset, and a long bubble is formed. Out of this range, reattachment occurs shortly after transition, and a short bubble is observed. The literature also reports that vortex and feedback mechanisms can also play a role in the bubble bursting. In the view of the current author, the investigation of the bubble formation

process can provide valuable insights to help describe the bursting process.

In the last decades, the extensive use of PIV techniques to measure flow fields has clarified many aspects of LSBs. An example of velocity profiles measured with this technique in an LSB is illustrated in Figure 2.5. Lengani et al. (2014) [15], used PIV measurements to study the vortex-shedding behavior associated with an LSB. For this purpose, the author applied a phase-identification technique to reconstruct the time-resolved shedding process, and then used POD to extract coherent structures. The results indicate that, in the rear portion of the bubble, about 70% of the total kinetic energy of the velocity fluctuations arises from turbulent activity, while the remaining 30% is associated with coherent motions induced by the large-scale vortical structures. Almutairi et al. (2016) [7], applied dynamic mode decomposition to a large-eddy simulation of a NACA-0012 airfoil operating near stall. Their analysis revealed two dominant modes. One is a low-frequency oscillatory mode, and the other is a high-frequency mode associated with trailing-edge vortex shedding. The results also indicated that acoustic feedback from the trailing edge can play a role in triggering earlier transition and in driving the reattachment of the separated flow. Michelis et al. (2017) [19], examined the flapping and bursting dynamics of a LSB, analyzing the spatial and temporal behavior of a recirculation bubble subjected to two-dimensional impulsive forcing using PIV measurements combined with linear stability theory. Lengani et al. (2017) [8], investigated the Reynolds stress components from a time-resolved PIV experiment of a LSB over a flat plate in a water tunnel using POD. The author characterized the bubble dynamics and, by means of model order reduction, identified the contributions of low-frequency motion of the separated shear layer, vortex shedding, and the development of finer scales in the rear part of the bubble to turbulence production. Yarusevych and Kotsonis (2017) [21], used PIV to characterize both the steady and transient response of a LSB forming on a NACA-0012 airfoil in a wind tunnel to two-dimensional, periodic flow perturbations. Their findings suggested that the evolution of the LSB is closely related to the formation of shear-layer roll-up vortices.

Since the seminal work of Gaster (1968) [1], it is well known that shear layer instabilities are essential for the vortex formation and consequently the bubble dynamics. Therefore, a brief survey of works devoted to investigating flow instabilities in the presence of laminar separation bubbles is provided in the next section.

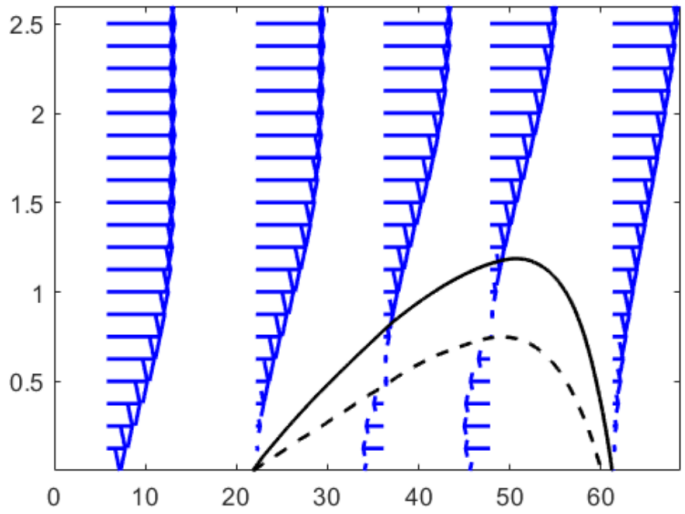

Figure 2.5: Velocity profiles of a LSB. Full line is the zero streamline, and pointed line is the zero velocity line. Image extracted from Pereira et al. (2023) [71]

.

2.1.2 About the instability

Dovgal et al. (1994) [10], presented a review of the instabilities and transitional phenomena involved in boundary-layer transition, including receptivity of separated flows to external disturbances, linear instability, and nonlinear wave interactions. Their work provided comments on feedback mechanisms and the control of laminar separated flows, focusing on how external excitation influences transition and, consequently, the bubble topology. According to Dovgal et al. (1994) [10], in a scenario of "quiet" free-stream conditions, the LSB unsteadiness and transition originate from the growth of initially small-amplitude flow disturbances. Indeed, since Gaster's [1] works in 60´ and 70´, it has become clear that the LSB is highly sensitive to such small-amplitude disturbances upstream to the bubble. One reason is that the whole bubble, including its laminar portion, can be influenced by the location of turbulence onset. In fact, a change in the transition location can modify the bubble topology and, hence, the base flow profiles in the bubble vicinity [10]. Thus, scenario can somehow represent a closed-loop system similar to the conjecture proposed by Horton (1968) [2].

According to the linear stability analysis presented by Gaster (1967) [1], low-frequency disturbances become less unstable than high-frequency ones right downstream of the separation point. Gaster (1967) [1], examined the

evolution of instability waves excited by a localized source. The results show that far from the source, the excited disturbances corresponded to eigenmode solutions of the instability problem. In addition, according to Dovgal et al. (1994) [10], at the separation, the incoming Tollmien–Schlichting (T-S) wave can be transformed into eigen-oscillations of the separation bubble (Kelvin Helmholtz modes).

Serna and Lázaro (2014) [16], examined the evolution of perturbations in the laminar portion of the shear layer using hot-wire anemometry and velocity. Their findings indicated that the characteristic non-dimensional frequency, which is similar to the most unstable frequency found in the shear layer, is weakly dependent on the Reynolds number, suggesting an inviscidly unstable shear-layer. For regions very close to the separation, Serna and Lázaro (2014) [16], compared the experiments against linear stability calculations. The results suggest that parallel-flow assumptions can somehow capture the main features of the instability modes in that region. This is interesting for simplified calculations and for the development of reduced-order models for engineering applications.

Ducoin et al. (2016) [11], analyzed the various physical mechanisms governing the transition to turbulence in a separated boundary layer over an airfoil at low incidence. The study considered a flow over an SD7003 wing section at an angle of attack $\alpha = 4°$, with Reynolds numbers ranging from $Re = 2 \cdot 10^3$ to $Re = 10^4$. They compared numerical simulations against experimental measurements, focusing on instability mechanisms in the separated region and the near wake. The results indicated that the shedding vortices are related to the K-H disturbances but at subharmonic frequencies of the von Kármán instability. Similar findings are reported in the work of Michelis et al. (2017) [19], where the roll-up vortices shed in the aft region of the LSB could be traced back to the convective amplification of T–S waves within the boundary layer upstream of the separation point. According to Dovgal et al. (1994) [10], and Yarusevych and Kotsonis (2017) [21], nonlinear interactions become important once the amplitude of streamwise velocity fluctuations reaches about 10%–20% of the free-stream velocity near the vortex roll-up location. Although the LSB appears well defined in a time-averaged sense (Figure 2.3), the physical processes governing reattachment are complex, three-dimensional, and highly unsteady [30]. According to Rodríguez, and Theofilis (2010) [70], there are both two- and three-dimensional instability mechanisms involved in the flow dynamics, and some three-dimensionality can

appear already at the linear region of the bubble.

There is still another mechanism that can be dominant in cases of bubbles with strong recirculation. Rodríguez, et al. (2013) [73], and Avanci et al. (2019) [53], identified that absolute mechanisms are relevant for these scenarios. Avanci et al. (2019) [53], found that on average, a secondary bubble embedded within the primary laminar separation bubble, implying that the flow is absolutely unstable according to a geometric criterion. Under conditions of absolute instability, the self-sustained unsteadiness within the bubble propagates upstream inside the recirculation region.

Most of LSB findings are reported for steady environmental conditions. However, variations of these conditions are inherent to practical application and this adds even more degrees of freedom to the problem. Next, a review of a few works available in the literature for this scenario is presented.

2.1.3 Laminar separation bubble in an unsteady environment

Most investigations of LSBs reported in the literature focus on the quasi-steady or quasi-permanent regime [71], while the transient behavior following the introduction of artificial disturbances has received comparatively little attention [21]. Toppings and Yarusevych (2024) [27], noted that prior studies of LSBs in unsteady flows have revealed structural and dynamical features that differ from those observed under quasi-steady operating conditions. According to Michelis et al. (2017) [19], because the transition process associated with LSBs is highly sensitive to environmental disturbances, variations in background disturbances, such as a low-pressure turbine blade passing through the wake of upstream stages (Figure 2.6) can impact a turbine's performance. This includes the stall onset, lift, drag, and noise emission.

The limited attention to this topic is mainly because experimental investigations of such transients are challenging, owing to strict demands on the measurement system's temporal resolution and phase-locked measurements [21]. In contrast, for numerical studies these transients would require long simulation times for extracting flow statistics and can be computationally very expensive.

Gungor et al. (2012) [14], investigated, using direct numerical simulation

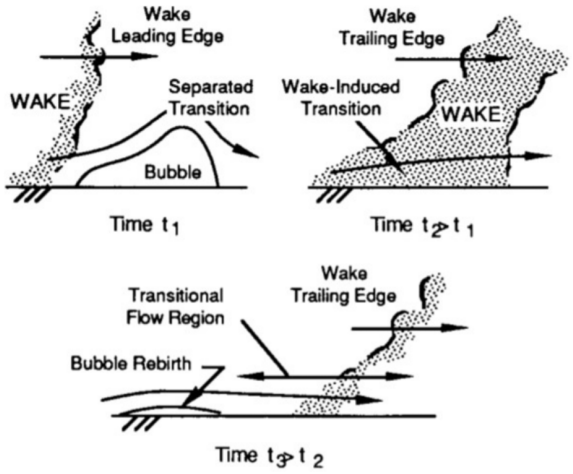

Figure 2.6: Process of suppression and formation of a laminar separation bubble. (Top left) The wake is upstream of the LSB in an instant t_1. (Top right) The wake induce early transition of the boundary layer and the bubble is suppressed. (Bottom) The wake is downstream of the LSB and the LSB restarts to form. Extracted from Mayle (1991) [66]

.

(DNS), a boundary layer flow over a flat plate disturbed by wakes, with a streamwise pressure distribution resembling that on the suction side of typical low-pressure turbine blades. The goal was to improve the understanding of flow physics in turbine passages and to provide reference data for advanced design methods and turbulence modeling. Those authors evaluated how the separated boundary layer responds to passing wakes, both in terms of frequency and wavelength. They found that the forcing frequency strongly influences the instantaneous positions of separation and reattachment. Michelis et al. (2017) [19], investigated the spatial and temporal response characteristics of a LSB to impulsive forcing by the means of time-resolved PIV and linear stability theory. The results of this study shed light on the response of laminar separation bubbles to impulsive forcing, providing insight into the attendant changes of flow dynamics and the underlying stability mechanisms.

Toppings and Yarusevych (2024) [27], experimentally investigated the transient dynamics associated with the formation and bursting of a laminar separation bubble on a rectangular NACA-0018 wing. The models were subjected to ramp variations in free-stream velocity, driving the flow to alternate between a regime in which a laminar separation bubble forms with reattachment and a regime without reattachment. Lift measurements and PIV data were used to relate the unsteady flow development to the associated aerodynamic loads. The study found out that the lift coefficient of the airfoil exhibits substantial hysteresis for the bubble formation and bursting. In contrast, the

transient lift shows less hysteresis, gradually changing due to slower spanwise expansion and contraction of the separated flow region relative to the airfoil.

Toppings and Yarusevych (2025) [28], carried out experiments on an airfoil and a wing model at aerodynamically low Reynolds numbers subjected to transient variations in angle of attack at multiple pitch rates and changes in Reynolds number. During this changes, lift force and PIV measurements were collected to analyze the link between LSB bursting and formation and the resulting transient aerodynamic loads. As the angle of attack increased, the LSB moves upstream prior to rapidly bursting, whereas for a decrease of Reynolds number, the LSB undergoes a more gradual monotonic increase in length prior to bursting. The process of LSB formation is less sensitive to the type of imposed change in operating conditions. Results also indicate that the spanwise flow development is also insensitive to the type of imposed transient during LSB bursting and formation.

Horna (2024) [63], examined the formation mechanism and asymptotic growth of an LSB, starting from the initial onset of boundary-layer separation up to the point where the bubble attained a quasi-steady state. The data were obtained using time-resolved PIV. The experimental setup consisted of a flat plate placed in a water tunnel with a convergent–divergent configuration to reproduce the pressure gradients typical of low-pressure turbines. Furthermore, to the best of the author's knowledge, the Horna (2024), [63], dataset is unique in capturing the asymptotic growth and formation of LSBs at high temporal and spatial resolution. The experimental results on the bubble-formation process from that thesis are revisited here and analyzed in the context of dynamics systems and reduced-order modeling.

2.2 Reduced order model for fluid flows

Solutions of the Navier–Stokes equations and experimental investigations leads to accurate, high-fidelity predictions for many fluid-dynamic problems. However, both approaches entail substantial computational and financial costs [26]. As a result, systematically identifying effective actuation and sensing strategies, as well as designing suitable control laws, becomes prohibitively expensive [33]. These challenges have motivated the development of reduced-order models [37], which offer an efficient framework for revealing dominant physical mechanisms, performing rapid parametric or exploratory studies of actuation concepts, and rigorously applying methods from control theory and dynamical systems [32]. This section focuses on the POD–Galerkin approach for modeling fluid flows.

2.2.1 The Proper Orthogonal Decomposition for fluid flows

The POD of a covariance matrix is a well-established concept, commonly known as the Karhunen–Loève expansion in pattern recognition and as principal component analysis (PCA) in statistics. An overview of the POD technique for the dynamical characterization and model-order reduction of linear and nonlinear mechanical systems is provided in Kerschen et al. (2005) [40].

According to Sirovich (1987) [45], two distinct developments have modified Taylor's classical statistical framework for turbulence. On the experimental side, a wealth of data now supports the presence of coherent structures; on the theoretical side, the application of dynamical systems theory to turbulent flows indicates that they evolve on relatively low-dimensional manifolds or attractors. Within this setting, modal decomposition techniques offer a powerful means to address these issues. This aligns with the common perspective that chaotic, dissipative dynamical systems ultimately evolve toward a *strange attractor* of comparatively low dimension. Consequently, the method yields a practical and, in a certain sense, optimal characterization of the attractor. Modal analysis is widely employed to interpret the dynamic response of structures; however, a primary concern among structural dynamicists is that its range of validity is essentially confined to linear systems. Thus, its capability to capture the dynamics of complex flows is not known a priori.

POD is a multivariate statistical technique designed to obtain a compact representation of data, which can be used for two main objectives: model order reduction and feature extraction [40]. As noted by Couplet et al. (2005) [34], POD provides a theoretical, post-processing framework for identifying coherent flow structures, thereby enabling their description and analysis. It operates by compressing a collection of numerical realizations into a reduced set of orthogonal basis functions that, when appropriately combined, retain the most significant information [43].

The signal-dependent character of the method can be regarded as one of its main drawbacks, as noted by Kerschen et al. (2005) [40], since it prevents us from assigning a general physical meaning to the extracted modes. Nonetheless, it is important to recognize that, in certain specific situations, the modes may resemble, or even exactly match, the physical mode shapes. Another aspect that should be highlighted is that, because POD eliminates linear correlations between variables, it is only responsive to second-order

statistics and does not, in general, guarantee statistical independence [40].

Lumley (1967) [46], first introduced and developed the POD method within fluid mechanics to identify coherent structures in turbulent flows, and Sirovich (1987) [45], later proposed the snapshot (or strobe) method, which enabled its use for machinery power applications. According to Berkooz et al. (1993) [56], a major advantage of POD is its statistical basis, whose analytical underpinnings provide a clear picture of both its strengths and its limitations. The method allows the extraction of spatial and temporal structures from a turbulent field, selected as essential according to predefined criteria, and thus offers a rigorous mathematical framework for their characterization [75]. Consequently, POD is not only a tool for analyzing and synthesizing flow data obtained from experiments or simulations, but also a means to derive, from the Navier–Stokes equations, low-dimensional dynamical models that describe the interaction of these key structures [76]. As stated by Kerschen et al. (2005) [40], the central idea behind POD is to condense a large set of interdependent variables into a much smaller set of uncorrelated variables, while preserving as much of the original variability as possible. Today, POD and many variants based on this idear are widely used in fluid mechanics [31].

The appeal of POD stems from the fact that it is a linear procedure, grounded in the spectral theory of compact, self-adjoint operators. As noted in Berkooz et al. (1993) [56], although it does not involve the same kind of physical distortion as linearization techniques, its fundamentally linear character constrains its capabilities. It is important to emphasize that POD does not impose any assumption of linearity on the underlying problem to which it is applied. In this sense, it is as indiscriminate, and as broadly applicable, as Fourier analysis. This "robustness makes it a safe haven in the intimidating world of nonlinearity," as Lumley (1967) [46], remarks. According to Lengani et al. (2014) [15], POD is now a well-established mathematical tool, extensively employed to identify coherent structures embedded in fluid flows.

Following Kerschen et al. (2005) [40], the linear character of the method can be limiting for certain data sets. For instance, when the data lie on a nonlinear manifold, the method tends to overestimate the intrinsic dimensionality. A further drawback is that POD attempts to represent the entire data set using a single set of global features, whereas in practice a complex data set often exhibits distinct properties in different regions of the space.

This motivates the adoption of local features to capture qualitatively different portions of the data more efficiently.

According to Kerschen et al. (2005) [40], the modes obtained from POD can be used both for model order reduction, by projecting high-dimensional data onto a lower-dimensional subspace, and for feature extraction, by uncovering relevant coherent structures embedded in the data. POD yields a low-rank basis that forms a hierarchy of orthonormal modes [22], which can be proven to be optimal in the sense that the associated time-averaged energy residual is minimal among all possible expansions with N modes [32, 33]. Hence, it is optimal with respect to energy content in a least-squares sense [40].

In the context of LSB, Lengani et al. (2014) [15], employed a finite number of POD modes to build a low-order model that captures the dynamics of the generation and convection of coherent structures shed due to shear-layer roll-up, and to determine the spatial and temporal distribution of other velocity fluctuations not directly linked to the shedding process. The author further reported that the energy content of the first POD mode is significantly higher than that of the second mode. As a result, the first two modes are uncoupled, whereas a pairing behavior appears to re-emerge for the third and fourth modes. He also noted that the K–H instability begins to trigger the shedding of large vortical structures as a consequence of shear-layer roll-up, which is clearly evidenced by the onset of significant values in the spatial distributions of the wall-normal velocity component POD modes, whose wavelength matches that of the instability.

Michelis et al. (2017) [19], applied POD to decompose the fluctuating field into eigenfunctions. The results indicated that, for both the unforced and forced configurations, approximately 85% of the total estimated modal energy is contained in the first four POD modes. The author further interpreted these modes: the first is linked to the flapping motion of the shear layer, the second corresponds to the rapid contraction and reformation of the laminar separation shear layer, and the third and fourth are related to shedding dynamics and the convection of the imposed disturbances.

Lengani et al. (2017) [8], investigated the Reynolds stress components obtained from a time-resolved PIV experiment of an LSB developing over a flat plate in a water tunnel, using POD as the analysis tool. The author characterized the flow dynamics and, through a reduced-order framework,

clarified the contribution of the low-frequency motion of the separated shear layer, the vortex-shedding process, and the emergence of finer scales in the downstream portion of the bubble to turbulence production. The effectiveness of POD in detecting and distinguishing the various dynamical mechanisms responsible for flow oscillations was assessed. In particular, for the LSB case, POD can distinctly separate the low-frequency behavior of the separated shear layer from the K–H vortex-shedding process, as well as isolate the small-scale structures developing in the reattachment region.

Dellacasagrande et al. (2023) [9], employed POD to examine the bubble mean flow in a quasi-steady regime and its response to variations in the influencing parameters. In doing so, he obtained a low-dimensional representation of the statistical behavior of a LSB with respect to the primary influencing parameter, using a modal decomposition of a large time-averaged ensemble. The study also demonstrated that an LSB can be distinguished according to its location in the POD state space, thereby highlighting the ability of the POD technique to deliver a data-driven classification of the LSB state.

Indeed, the methodology is very suitable for the analysis of LSB PIV data in the present context, and it will be employed here in the variant form of POD-Galerkin approach [32, 39].

2.2.2 The POD-Galerkin approach

Owing to rapid advances in computational technology, data-driven modeling techniques have gained substantial popularity and have been adopted across numerous research domains, including fluid dynamics. The combined effects of strong nonlinearity, high dimensionality, and the rich dynamical behavior of fluid mechanical systems emphasize the need for a trade-off between model accuracy, dynamical representation, cost, and simplicity. This motivated the development of ROMs, which are identified directly from experimental or high-fidelity simulation data [37]. According to Noack et al. (2004) [33], the systematic exploration of effective actuation and sensing strategies, as well as subsequent control design, is prohibitively expensive when performed solely within CFD frameworks. Consequently, low-dimensional flow models are sought as practical tools. As further emphasized by Noack et al. (2003) [32], such models provide a suitable test bed for elucidating key physical mechanisms, facilitate rapid exploratory studies of flow actuation, and enable the application of modern control theory and dynamical systems methods [77]. Thus, these coherent-

structure-based descriptions bridge the gap in the theoretical spectrum between analytical theories and high-dimensional, high-fidelity simulations. According to Deng et al. (2020) [35], ROMs serve multiple purposes. For example, ROMs enable a deeper understanding of the underlying physical mechanisms in a given flow configuration by identifying the low-dimensional manifold on which the system dynamics evolve. Furthermore, ROMs provide computationally efficient surrogates for predicting the system's forward temporal evolution. Such surrogates can be exploited for control applications [61, 62, 60], substantially reducing the computational cost of *online* deployment by obviating the need to repeatedly perform expensive simulations or experiments [26].

As underlined by Hijazi et al. (2020) [43], despite the recent growth in available computational power and the development of novel numerical algorithms, the direct numerical solution of the governing equations by means of classical discretization techniques, such as finite difference, finite element, finite volume, or spectral element methods, may, for several reasons, be impractical or inefficient. This limitation becomes particularly evident in settings such as real-time control problems, where computational cost is a constraint, or in multi-query contexts, where a quantity of interest must be evaluated repeatedly across a large number of parameter or input configurations, as in optimization, uncertainty quantification, or other repetitive computational scenarios. In such cases, the computational cost of standard high-fidelity numerical solvers can become prohibitive.

ROMs have proved effective in addressing these challenges by significantly reducing computational time and yielding substantial speed-ups while preserving acceptable accuracy.

According to Rempfer (2003) [55], Galerkin methods are a natural candidate for describing globally synchronized dynamics, such as vortex shedding in the near wake. The dimension and properties of the resulting Galerkin model depend strongly on the choice of the expansion modes in the Galerkin approximation, which can be classified in terms of mathematical, physical, and empirical approaches [32]. As observed in Brunton et al. (2016) [22], fundamental physical insight can provide a reasonable selection of nonlinear functions and measurement coordinates. The choice of appropriate coordinates to simplify the dynamics has long been recognized as essential, as exemplified by Lagrangian and Hamiltonian mechanics.

Moreover, many high-dimensional systems of interest evolve on a low-dimensional manifold or attractor that can be accurately approximated using a low-rank basis. For instance, when data are collected from a high-dimensional system, a low-rank approximation can be obtained through dimensionality-

reduction techniques such as POD [22]. As argued in Noack et al. (2003) [32], since POD is optimal in an energetic sense, a Galerkin approximation constructed from its modes can be expected to be highly efficient, especially for periodic flows.

According to Luchtenburg et al. (2009) [36], the Galerkin method, and, in particular, the POD–Galerkin model, is especially attractive and widely employed, owing to its optimal efficiency in representing the dynamics of globally dominant coherent flow structures. The POD–Galerkin framework is explicitly constructed to neglect small-scale structures and convective effects. As noted in Couplet et al. (2005) [34], since separated flows are often governed by a relatively small number of coherent structures, it is advantageous to employ spatial POD modes as basis functions in a Galerkin projection in order to derive a system of ordinary differential equations (ODEs) that approximates the full flow dynamics. Consequently, after truncating the POD modal basis to retain only the leading modes, a reduced-dimensional ODE system can be obtained.

According to Noack et al. (2003) [32], Noack et al. (2004) [33], the adopted Galerkin approximation can, at best, replicate the reference simulation and is often unable to represent the flow dynamics at different forcing amplitudes or frequencies. As discussed in Schlegel and Noack [38], such models tend to be fragile, in the sense that variations in system parameters can lead to unphysical, divergent solutions, at least for specific subsets of initial conditions. Consequently, parameter identification becomes a highly sensitive and nontrivial task, and a priori knowledge of the long-term behavior of Galerkin models for all admissible initial conditions is highly desirable. Furthermore, it should be emphasized that reconstructing the original system matrix from a reduced-order approximation inevitably entails a loss of resolution [26]. While this resolution reduction can be beneficial for noise filtering, it is crucial to select a sufficiently high model order to ensure that the dominant and physically relevant flow features are accurately captured.

In this study, we adopted the methodology proposed by Noack et al. (2004) [33], in which the POD–Galerkin framework is integrated with system identification techniques. This combined approach enables the empirical determination of the model coefficients directly from the available measurements, rather than deriving them in a strictly analytical manner.

2.2.2.1 Sparse Identification of Nonlinear Dynamics

Identifying dynamical systems and inferring their governing equations directly from data is a central challenge across several disciplines, including mathematics and physics, with a particularly rich history in fluid dynamics [39, 22]. Recent advances in machine learning have greatly expanded the ability to infer governing dynamics from data alone. However, many of these approaches, most notably neural networks, often suffer from limited interpretability and a high propensity for overfitting, thereby compromising their predictive capability [22, 24].

The work of Brunton et al. (2016) [22], addresses the problem of dynamical system discovery from the perspective of sparse regression and compressed sensing, proposing the SINDy framework. This methodology relies on the assumption that only a small number of terms are dynamically relevant, implying that the true governing equations are sparse in the space of candidate functions. As shown by Champion et al. (2020) [23], because SINDy is formulated as a sparsity-promoting linear regression problem, it naturally accommodates the incorporation of partial physical knowledge, such as symmetries, constraints, and conservation laws.

Furthermore, as noted by Loiseau and Brunton (2018) [39], the structure of the inferred system can typically be constrained using prior information about the governing equations, for instance, those obtained via Galerkin projection. To perform such a procedure efficiently, a reduced-order representation of the data field is usually required [26].

In summary, SINDy employs sparse regression to identify the minimal set of terms in the governing equations necessary to represent the observed data with high fidelity. The Figure 2.7 summarizes the method by exemplifying the identification of the Lorenz equations. The outcome is a parsimonious model that achieves a balance between accuracy and complexity, thereby mitigating overfitting while maintaining interpretability [22].

2.2.2.2 Application POD-Galerking in the literature

Noack et al. (2003) [32], proposes a generalized Galerkin model for the incompressible, viscous Navier–Stokes equations that combines the respective advantages of empirical and mathematical Galerkin approaches. The model leverages the accuracy of empirically derived modes while extending the range of applicability and improving robustness through elements of the mathematically derived formulation. The key modification consists of incorporating a *shift*

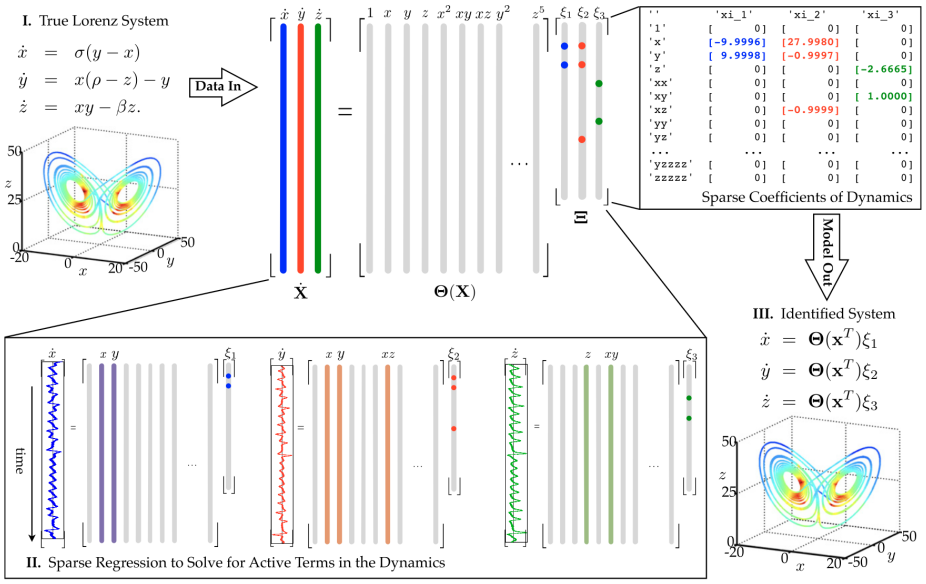

Figure 2.7: Schematic of SINDy algorithm, demonstrated on the Lorenz equations. Data collected from the system, including a time history of the states $\mathbf{X}$ and derivatives $\dot{\mathbf{X}}$. Next, a library of nonlinear functions of the states, $\mathbf{\Theta}(\mathbf{X})$, is constructed. This nonlinear feature library is used to find the fewest terms needed to satisfy $\dot{\mathbf{X}} = \mathbf{\Theta}(\mathbf{X})\mathbf{\Xi}$. The few entries in the vector $\mathbf{\Xi}$, solved for by sparse regression, denote the relevant terms in the right-hand side of the dynamics. Parameter values are $\sigma = 10$, $\beta = 8/3$, $\rho = 28$, $(\mathbf{x}_0, \mathbf{y}_0, \mathbf{z}_0)^T = (-8, 7, 27)^T$. The trajectory on the Lorenz attractor is colored by the adaptive time step required, with red indicating a smaller time step. Extracted from Brunton et al. (2016) [22].

mode, ensuring that the Galerkin expansion accurately represents the unstable steady solution. In that study, a low-dimensional model of the cylinder wake is developed, in which the inclusion of the shift mode yields a substantially improved prediction of the transient dynamics. The author argues that analogous models can be expected to perform well for other absolutely unstable flows.

In Noack et al. (2004) [33], a framework is developed for representing actuation effects in low-order empirical Galerkin models of incompressible flows, and a flow-control strategy is proposed based on these extended models and on the design of dissipative feedback controllers. Couplet et al. (2005) [34], derives a calibrated reduced-order POD–Galerkin system for a two-dimensional flow past a square cylinder and for a three-dimensional flow over a backward-facing step. Deng et al. (2020) [35], propose a least-order model based on the instabilities undergone by the flow as the Reynolds number is increased. Luchtenburg et al. (2009) [36], introduces a low-dimensional Galerkin model for the flow over a high-lift configuration, capturing natural vortex shedding, high-

frequency actuated flow with enhanced lift, and the transients between these regimes. The structure of the dynamical system is obtained from a generalized mean-field analysis. Steady-state and transient Unsteady Reynolds-Averaged Navier–Stokes (URANS) simulation data are used to construct the expansion modes and to calibrate the system parameters. The resulting model identifies the mean field as the mediator between high-frequency actuation and the low-frequency natural shedding instability. The model proposed in this note is based on the mean-field theory developed in Noack et al. (2003) [32]. Finally, Tadmor et al. (2011) [37], provides comprehensive guidelines for the implementation of Galerkin models across various classes of flows and application-specific requirements. In addition, Loiseau and Brunton (2018) [39], demonstrates the sparse Galerkin regression approach for two canonical configurations: the two-dimensional cylinder flow and the shear-driven cavity flow.

Building on these developments, a new data-driven Galerkin regression framework is formulated to identify nonlinear reduced-order models of fluid flows. The resulting models retain several advantageous properties of standard Galerkin projections, such as interpretability and ease of use, while eliminating the requirement for access to a high-fidelity N–S model for the projection step. It is shown that the inclusion of higher-order nonlinearities in the regression significantly improves the stability and accuracy of the resulting models, enabling them to capture the influence of truncated low-energy modes on the dynamics of the energetically dominant modes. To this end, Loiseau and Brunton (2018) [39], proposes a new implementation, based on the SINDy algorithm, that enables the incorporation of physical constraints, such as energy-preserving nonlinearities or symmetry conditions, directly into the identified equations. The Galerkin regression framework extends the original SINDy formulation by enabling user-prescribed constraints to be incorporated directly into the sparsity-promoting regression. These additional constraints can be employed to impose *a priori* known values of selected regression coefficients, to enforce intrinsic symmetries of the governing equations, or to guarantee specific physical properties, such as the energy-preserving nature of the quadratic nonlinearity in the Navier–Stokes equations.

Hijazi et al. (2020) [43], propose a reduced-order model specifically designed for turbulent flows in a finite-volume context. The method combines a projection-based technique with data-driven reduction strategies, in particular to approximate the eddy-viscosity solution manifold, together with a classical POD–Galerkin projection for the velocity and pressure fields.

Deng et al. (2020) [35], advance mean-field modeling by introducing the first lowest-order Galerkin model of an incompressible flow undergoing

two successive supercritical bifurcations of Hopf and pitchfork type. The resulting five-dimensional model successfully reproduces the phenomenology of the fluidic pinball configuration.

Girfoglio et al. (2022) [44], develop a POD–Galerkin-based reduced-order model for the efficient numerical simulation of the parametric N–S equations in streamfunction–vorticity formulation. The performance of the model is assessed on the vortex-merger benchmark and on a test case involving the geometry of the North Atlantic Ocean. Their model accurately captures the flow features, both in terms of reconstructing the temporal evolution of the flow field and in a parametric physical setting. Moreover, for the simplified vortex-merger problem, they report a substantial reduction in computational time.

Brunton et al. (2016) [22], integrated sparsity-promoting methodologies and machine learning with nonlinear dynamical systems theory to infer governing equations directly from noisy measurement data. The algorithm was demonstrated on a broad spectrum of benchmark problems, ranging from simple canonical systems, including linear and nonlinear oscillators and the chaotic Lorenz system, to fluid-structure scenarios such as vortex shedding behind an obstacle.

Zheng et al. (2019) [25], demonstrated the advantages of sparse relaxed regularized regression across a variety of regularized regression problems by benchmarking it against LASSO, matrix completion, total variation regularization, and group sparsity, and also provided an accompanying MATLAB software package. Sparsity-promoting regularization for regression problems remains important for obtaining actionable and interpretable models from data. Moreover, robustness, computational efficiency, and generalizability are essential properties for such algorithms to be broadly applicable across the sciences. Champion et al. (20200) [23], proposed a unified sparse optimization framework for dynamical system discovery that enables the simultaneous identification of governing equations, removal of corrupted training data, enforcement of known physical constraints, and detection of parametric dependencies in the equations. The SINDy-SR3 method can systematically incorporate constraints, yield robust models, and provide accurate estimates of nonlinear parameters. Silva et al. (2020) [24], developed a Python package for data-driven discovery of governing dynamical system models using the SINDy framework, thereby providing a centralized codebase in which many core SINDy capabilities are implemented to facilitate usability and standardization. Foster et al. (2022) [26], employed the SINDy algorithm to construct a ROM of the wake of a submerged cylinder undergoing prescribed oscillations, a

configuration closely related to vortex-induced vibration problems. The ROM was trained using 10 POD modes, achieving a relative error of 3.1% and a data reconstruction with a relative Frobenius norm error of 5%. The resulting ordinary differential equation model made possible to make conclusions about the physical system, for instance linearity and periodicity.

Marxen and Henningson (2011) [51], mentioned that accurate numerical simulations of the asymptotic growth of LSBs are computationally very expensive. Consequently, there remains a clear need for models capable of predicting LSB behavior, particularly in the transient regime [17]. Malmir et al. (2024) [31] demonstrated that the first three modes correspond to the low-frequency dynamics and are required in a reduced-order model to capture the associated low-frequency phenomena correctly. More recently, Horna (2024) [63], employed reduced-order modeling techniques to extract the dominant flow structures associated with bubble formation. According to Almutairi et al. (2016) [7], the incomplete understanding of LSB dynamics is hindering the development and implementation of effective control strategies to mitigate their undesirable effects. However, most of these control attempts are based on a limited comprehension of the underlying flow mechanisms. Panisset et al. (2023) [71], argued that, owing to the complexity of the phenomenon, no existing model is yet capable of accurately predicting the flow behavior over a broad range of parameters.

The current work aims to contribute to the problem of LSB modeling using the methods reviewed in this chapter. The next chapter is devoted to detailing the framework adopted to develop the research.

3
Methods

This chapter describes the methodological framework adopted to address the research problem. First, the chapter provides an overview of the experiments reported in Horna (2024), [63], that built the dataset used in the current work. Subsequently, the mathematical formulation of the Proper Orthogonal Decomposition and the Galerkin projection is detailed. To conclude, a resume of the data processing is provided.

3.1
Experimental approach and data acquisition

The data acquisition campaign was conducted by Horna (2024), [63], in the Fluids Engineering Laboratory of the Department of Mechanical Engineering at the *Pontifical Catholic University of Rio de Janeiro*, Brazil. The principal aspects of the experimental setup and procedure are summarized here to facilitate reproducibility. For a more comprehensive description and detailed analysis, the reader is referred to Horna (2024) [63].

The present investigation addresses the formation of a LSB in a two-dimensional boundary layer. For this purpose, Horna (2024) [63], obtained experimental data with both high spatial and temporal resolutions. The experiments were conducted in a low-turbulence, closed-return, open-surface water channel, with overall dimensions of 12 m in length, 2.7 m in width, and 2.3 m in height (see Figure 3.1). The facility operated with a water volume of 15 m^3, driven by a centrifugal pump powered by a 40 HP electric motor. According to Horna (2024) [63], the turbulence level is lower than 0.5%, which can be considered low for water channel facilities.

The experimental setup (Figure 3.2) comprised a transparent polycarbonate flat plate (3160 mm long, 830 mm wide, and 12 mm thick) installed inside the water channel. The test section had dimensions of 4000 mm in length, 860 mm in width, and 640 mm in height. The combination of the upper false walls and the flat plate formed a convergent–divergent channel, which generated a low-pressure region characterized by a suction peak followed by an adverse pressure gradient, qualitatively analogous to that observed on airfoils.

Upstream of the suction peak, a steel vibrating ribbon was installed,

spanning the entire width of the flat plate and actuated by an electromagnet mounted below the flat plate surface. This device was employed to control the boundary-layer disturbances upstream of the separation region. The vibrating ribbon plays a central role in the experiment, enabling the controlled reproduction of the LSB formation process from incipient separation to a quasi-stationary regime. The control system for the vibrating ribbon, encompassing both hardware and software components, was designed and implemented in the work of Horna (2024) [63].

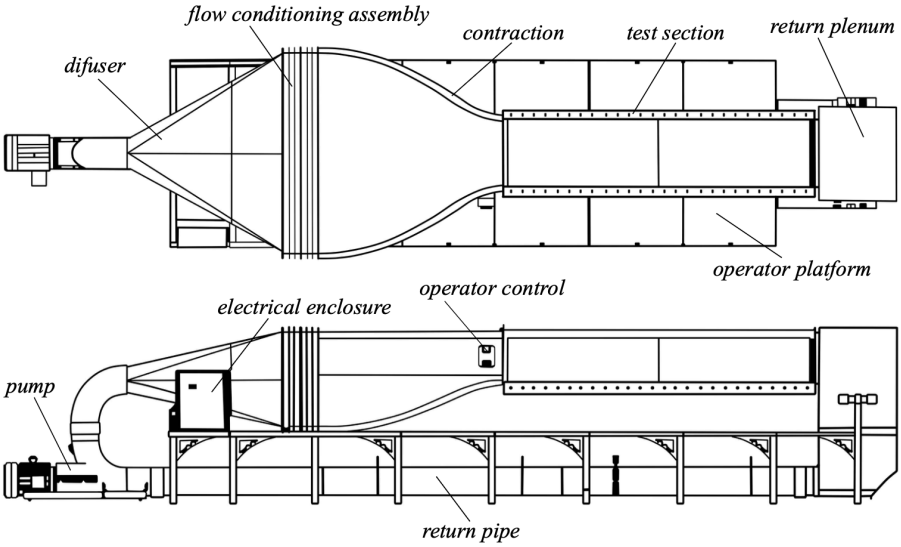

Figure 3.1: Front (bottom) and top (top) view of the closed return open water channel used by Horna (2024) [63]

To investigate the unsteady behavior of a laminar separation bubble in a two-dimensional boundary layer, its controlled asymptotic growth was measured using time-resolved PIV (Figure 3.3), which provides data with high spatial and temporal resolution. PIV is a well-established, non-intrusive, optical measurement technique for obtaining instantaneous velocity fields. By estimating the displacement of tracer particles that faithfully follow the fluid motion, the local flow velocity can be inferred. In this method, tracer particles are illuminated by a pulsed laser light sheet, and their positions are recorded by a camera at two consecutive time instants, t_0 and $t_0 + \Delta t$ [74]. Image processing algorithms are then applied to determine the displacements Δx and Δy of groups of tracer particles. Since the time interval Δt is known, the corresponding velocity components can be computed using the relations $u = \frac{\Delta x}{\Delta t}$ and $v = \frac{\Delta y}{\Delta t}$. Camera calibration enable conversion from image displacements to physical displacements.

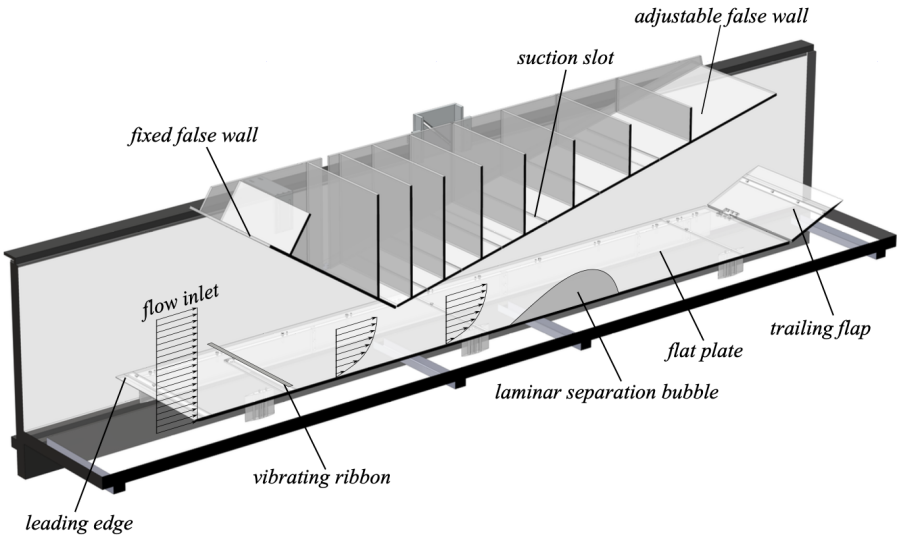

Figure 3.2: Section view of the experimental model. Image extracted from Horna (2024) [63]

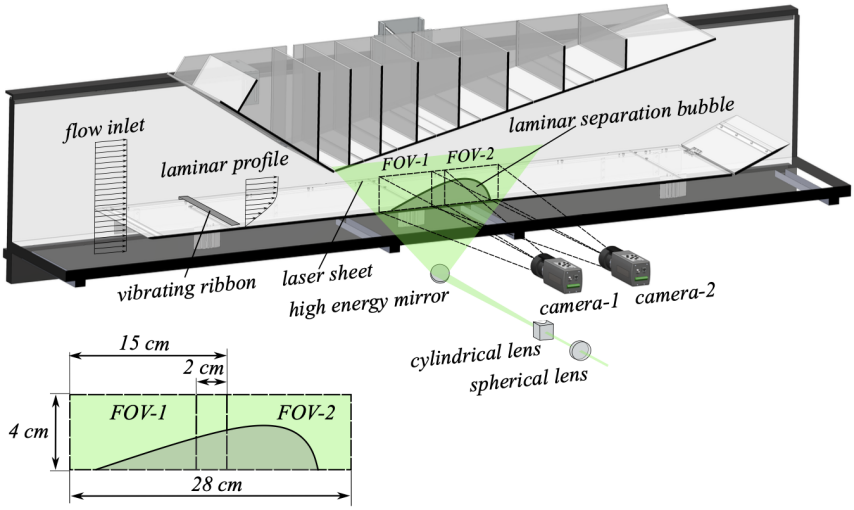

Figure 3.3: Section view of the PIV setup used. In the lower left part, an enlarged view of the total field of view (FOV). Image extracted from Horna (2024) [63]

The principal components and operating parameters of the time-resolved PIV system are summarized in Table 3.1.

The methodology adopted by Horna (2024) [63], consists of the application of double-frame/multi-exposure PIV in conjunction with a multi-pass method. This configuration was selected to enhance the effective seeding density in each recorded image and to enable refinement of the velocity field estimation, thereby yielding high-quality data while maintaining relatively

Laser system	LITRON LDV-300 series Nd:YAG
Measurement area	280 mm (length) × 40 mm (height)
High-speed cameras	Two CMOS Phantom Miro 340 cameras
Lenses	Nikkor lenses with focal length 105 mm, aperture $f/5.6$
Extender	PK-11 extension ring
Clock frequency	50 Hz
Resolution	2560 × 600 pixels
Seeding particles	Polyamide tracer particles with mean diameter 50 μm

Table 3.1: TR-PIV system characteristics.

short processing times.

In the double-frame/multi-exposure PIV configuration, the operation proceeds as follows: during the first laser pulse, the camera shutter is opened and the sensor records the particle positions, producing an initial exposure. While the sensor remains exposed, a second laser pulse illuminates the flow, capturing the particle positions at a later time instant within the same image. An analogous sequence is then repeated for the subsequent image pair, effectively doubling the number of particle images present in each snapshot. The principal limitation of this technique is a reduction in the maximum resolvable fluctuation frequency due to the extended effective exposure time. In the present experiment, however, the acquisition rate is sufficiently high such that the use of multi-exposure does not degrade the accuracy of the measured velocities.

For the PIV data processing, a multi-pass cross-correlation approach of image pairs (double-frame configuration) is employed, beginning with an interrogation window size of 64×64 pixels and concluding with a final pass using 16×16 pixel interrogation windows. The window overlap is set to 75%, thereby increasing the spatial resolution of the resulting velocity field. A comprehensive treatment of the PIV technique, including details of multi-exposure and multi-pass processing, is provided in Raffel et al. (2018) [74].

This procedure yields high-quality velocity fields. Figure 3.4 shows the evolution of the velocity profiles across the measurement domain, demonstrating the high spatial resolution of the acquired data. The velocity profiles shown at the bottom of Figure 3.4 indicate that the reverse flow very near the wall

was well resolved in the measurements. This is extremely difficult to capture on airfoils in wind tunnels due to the reduced size of the boundary layers. But in water channels, the task is less challenging because the boundary layer is thick and light reflections near the wall are reduced.

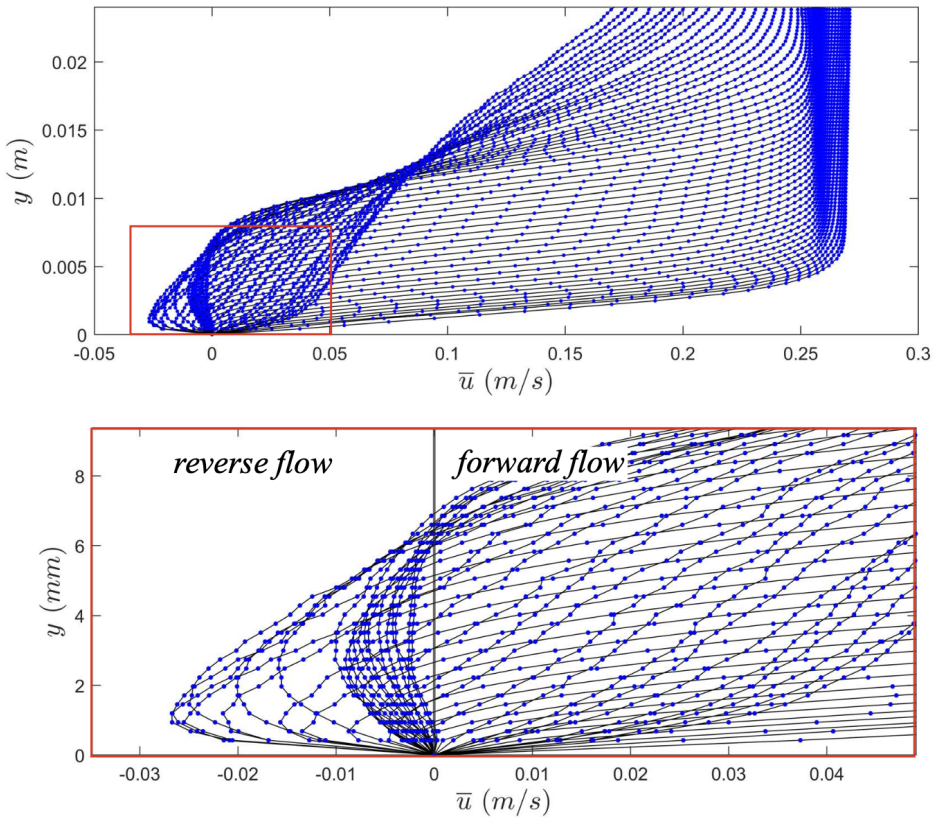

Figure 3.4: a) Velocity profiles taken along the entire length of the measurement field; b) enlarged image of the velocity profile velocity in the vicinity of the wall. Image extracted from Horna (2024) [63]

In the present investigation, the LSB was examined under forced disturbances. Consequently, the LSB developed in an environment characterized by small, well-controlled periodic velocity fluctuations. The experiment commenced by allowing a LSB to form under an undisturbed incoming flow with a streamwise velocity of 0.15 m/s at the inlet of the test section. After the bubble reached a quasi-steady state, the vibrating ribbon was actuated to oscillate with a high amplitude (experimentally determined by Horna (2024) [63]) at the most unstable frequency of the LSB, $f_{vb} = 2.5$ Hz.

At sufficiently high oscillation amplitudes, the device triggered the boundary layer transition to a turbulent regime. Under these conditions, the boundary layer remained attached to the surface fully suppressing the separation bubble. This forced turbulent state was maintained for 15 seconds to

ensure the complete elimination of the bubble. Subsequently, the oscillation amplitude of the vibrating ribbon was abruptly reduced to a small value, low enough to permit boundary-layer separation while still high enough to impose a known and controlled disturbance level exceeding that of the natural background fluctuations, as detailed in 4.1. In this work, only data related to the asymptotic growth of the LSB are analyzed.

Following this adjustment, the LSB reinitiated its formation process, evolving from separation to a quasi-permanent regime, during which the velocity field was captured as previously described. For this study, approximately 2×10^5 images were acquired, analyzed, and processed using in-house image processing codes. To enhance the statistical significance of the measurements, the experiment was repeated 20 times, and ensemble averaging was employed.

3.2 Proper Orthogonal Decomposition

According to Kerschen et al. (2005) [40], the central concept of POD is to compress a large set of mutually dependent variables into a much smaller collection of uncorrelated variables, while preserving as much as possible of the original variability. This is achieved by performing an orthogonal transformation of the basis formed by the eigenvectors of the sample covariance matrix, and then projecting the data onto the subspace spanned by the eigenvectors corresponding to the largest eigenvalues. As a result, the signal components are decorrelated and the variance is maximized.

We performed a modal decomposition of the transient velocity fields, representing the formation of the LSB, to reduce its dimensionality. POD was selected because it is optimal in the sense that it minimizes the mean squared error between the original signal and its reduced linear approximation, which is expressed in terms of an orthonormal basis. Consequently, it satisfies the conditions required for constructing a ROM via Galerkin projections.

Accordingly, given the velocity field data $\mathbf{u}(\mathbf{x}, t)$, it can be expressed as the sum of the mean velocity field $\bar{u}(\mathbf{x})$ and the fluctuating component $\mathbf{u}'(\mathbf{x}, t)$ (3-1), following the method of snapshots:

$$\mathbf{u}(\mathbf{x}, t) = \bar{\mathbf{u}}(\mathbf{x}) + \mathbf{u}'(\mathbf{x}, t) \tag{3-1}$$

Because the fluctuation term $\mathbf{u}'(\mathbf{x}, t)$ is the only quantity that depends on time, it is approximated using POD as follows (3-2):

$$\mathbf{u}'(\mathbf{x}, t) = \sum_{k=1}^{\infty} a_k(t)\Phi_k(\mathbf{x}) \tag{3-2}$$

where $a_k(t)$ represents the temporal evolution of the amplitude and $\Phi(\mathbf{x})$ denotes the spatial function.

To determine the spatial modes $\Phi_k(\mathbf{x})$ and the temporal coefficients $a_k(t)$, we employ singular value decomposition (SVD) (3-3), which is directly related to the POD method (see Kerschen et al. (2005) [40], for a detailed mathematical description).
According to Luchtenburg et al. (2009) [36], a commonly used mode basis is obtained from POD, which is optimal in the sense that it extracts the most energetic structures from a given flow field.

The SVD of $\mathbf{u}'(\mathbf{x}, t)$ yields the factorization (3-3).

$$\mathbf{u}' = \Phi \Sigma \mathbf{V}^T \tag{3-3}$$

Where Φ denotes the left-singular matrix whose columns Φ_k form an orthonormal basis for the spatial content, Σ is a square diagonal matrix whose diagonal entries are the singular values σ_k, and V is the right-singular matrix whose columns v_k represent the temporal behavior of the structure. Hence, SVD is advantageous because the time-dependent information is encoded in the columns of $\mathbf{V}$ [40]. In particular, each column v_k describes the temporal modulation of the associated spatial mode Φ_k, scaled by the corresponding singular value σ_k. Finally, the fluctuation field can be approximated as (3-4).

$$\mathbf{u}'(\mathbf{x}, t) = \sum_{k=1}^{\infty} [\Sigma_k V_k^T(t)] \Phi_k(\mathbf{x}) \tag{3-4}$$

3.3 Galerkin projection model

We derive a Galerkin ROM to characterize the asymptotic growth of the laminar separation bubble. As a starting point, we consider the dimensionless incompressible N–S equations (3-5), following the formulations in Noack et al. (2003) [32], and Deng et al. (2020) [35].

$$\frac{\partial \mathbf{u}}{\partial t} + \nabla \cdot \mathbf{u} \otimes \mathbf{u} = \frac{1}{Re} \Delta \mathbf{u} - \nabla p \tag{3-5}$$

$$\nabla \cdot \mathbf{u} = 0 \tag{3-6}$$

The Galerkin method is formulated with respect to the inner product defined on the Hilbert space of square-integrable vector fields, $\mathcal{L}^2(\Omega)$, over the observation domain Ω. The canonical (standard) inner product between $\mathbf{u}(\mathbf{x})$ and $\mathbf{v}(\mathbf{x})$ is given by (3-7).

$$(\mathbf{u},\mathbf{v})_\Omega := \int_\Omega \mathbf{dA}\ \mathbf{u}(\mathbf{x}) \cdot \mathbf{v}(\mathbf{x}) \tag{3-7}$$

A conventional Galerkin approximation employing a fundamental mode $\mathbf{u}_0$, for example, the base flow, and N orthonormal expansion modes $\mathbf{u}_i(\mathbf{x})$, $i = 1, \ldots, N$, associated with time-dependent amplitudes $a_i(t)$, can be expressed as follows (3-8)

$$\mathbf{u}(\mathbf{x}, t) = \mathbf{u}_0(\mathbf{x}) + \sum_{i=1}^{N} a_i(t)\mathbf{u}_i(\mathbf{x}) \tag{3-8}$$

Following Noack et al. (2003) [32], let $i = 1, \ldots, N$ denote the first N POD modes, and $a_i(t)$ their associated time-dependent Fourier coefficients, given by $a_i(t) = (\mathbf{u} - \mathbf{u}_0, \mathbf{u}_i)_\Omega$. Orthonormality implies (3-9):

$$(\mathbf{u}_i, \mathbf{u}_j) = \kappa_{i,j} \qquad i, j \in 1, ..., N \tag{3-9}$$

Where $\kappa_{i,j}$ equals zero when $i \neq j$, and equals one when $i = j$.

Projecting equation (3-8) onto equation (3-5) yields the linear-quadratic Galerkin system (3-10) ([41]).

$$\dot{a}_i = \tau \sum_{j=0}^{N} l_{ij}^{\tau} a_j + \sum_{j,k=0}^{N} q_{ijk}^{c} a_j a_k \tag{3-10}$$

Following Rempfer and Fasel (1994) [42], we introduce $a_0(t) = 1$. The coefficients $l_{ij}^{\nu} = (\mathbf{u}_i, \Delta\mathbf{u}_j)$ and $q_{ijk}^{c} = -(\mathbf{u}_i, \nabla \cdot \mathbf{u}_j \otimes \mathbf{u}_k)_\Omega$ represent the viscous and convective contributions of the N–S equations, respectively. Because all spatial modes satisfy the incompressibility constraint of the N–S equations, the pressure term vanishes under the inner product [36]. In what follows, the base flow, $\mathbf{u}_s$, is chosen as the fundamental mode, $\mathbf{u}_0$. Thus, $\mathbf{u}_0 = \mathbf{u}_s$. Consequently, $\mathbf{a}$=0 is a fixed point of (3-10), and the constant term $\frac{1}{Re} l_{i0}^{\nu} + q_{i00}^{\nu} = 0$ cancels out. Under these conditions, (3-10) can be reformulated as a linear–quadratic system of ODEs (3-11):

$$\dot{a}_i = \sum_{j=1}^{N} l_{ij} a_j + \sum_{j,k=1}^{N} q_{ijk} a_j a_k \tag{3-11}$$

where the linear coefficient is given by $l_{ij} = \frac{1}{Re} l_{ij}^{\nu} + q_{ij0}^{c} + q_{i0j}^{c}$ and the bilinear coefficient by $q_{ijk} = q_{ijk}^{c}$ for $i, j, k \in \{1, \ldots, N\}$.

3.4 Sparse Identification of Nonlinear Dynamics

The final step consisted of determining the linear and bilinear coefficients of the Galerkin model. To accomplish this, we employed a sparse model discovery method known as SINDy.

SINDy combines sparsity-promoting techniques with machine learning to infer governing equations from noisy measurement data for nonlinear dynamical systems. The only structural assumption is that the system dynamics are controlled by a small number of dominant terms, implying that the true equations are sparse within the high-dimensional nonlinear function space. A sparse regression framework is then used to identify the minimal set of terms in the governing equations that still provides an accurate representation of the data [22]. This sparse model discovery approach naturally balances model complexity and fidelity, thereby mitigating the risk of overfitting to the data [24].

A wide range of high-dimensional systems of interest evolve on a low-dimensional manifold or attractor that can be well represented by a low-rank basis Φ [39]. Here, the data correspond to a high-dimensional system $\mathbf{u}(\mathbf{x},\mathrm{t})$, for which a low-rank representation was obtained via POD as a dimensionality-reduction method. Considering a dynamical system of the form (3-12):

$$\dot{a}_i(t) = \mathbf{f}(\mathbf{a}(t)) \tag{3-12}$$

The vector $\mathbf{a}(\mathrm{t}) \in \mathcal{R}^n$ represents the system state at time t, and the function $\mathbf{f}(\mathbf{a}(\mathrm{t}))$ encodes the dynamical constraints governing the system's equations of motion.

In particular, SINDy approximates the dynamics sparsely using a library of candidate basis functions (3-13)

$$\mathbf{f}(\mathbf{a}(t)) \approx \sum_{k=1}^{n} \theta_k(\mathbf{a}(t))\xi_k \tag{3-13}$$

To identify the function $\mathbf{f}(\mathbf{a}(\mathrm{t}))$ from data, we first obtained the time series $\mathbf{a}(\mathrm{t})$ of the reduced-order state associated with the approximated field $\mathbf{u}'(\mathbf{x},\mathrm{t})$ via POD. The time derivative $\dot{\mathbf{a}}(t)$ was then computed numerically using a fourth-order differentiation scheme applied to $\mathbf{a}(\mathrm{t})$. The resulting samples were organized into two data matrices:

$$\mathbf{A} = \begin{bmatrix} \mathbf{A}^T(t_1) \\ \mathbf{A}^T(t_2) \\ \vdots \\ \mathbf{A}^T(t_m) \end{bmatrix} = \begin{bmatrix} a_1(t_1) & a_2(t_1) & \dots & a_n(t_1) \\ a_1(t_2) & a_2(t_2) & \dots & a_n(t_2) \\ \vdots & \vdots & \ddots & \vdots \\ a_1(t_m) & a_2(t_m) & \dots & a_n(t_m) \end{bmatrix} \tag{3-14}$$

$$\dot{\mathbf{A}} = \begin{bmatrix} \dot{\mathbf{A}}^T(t_1) \\ \dot{\mathbf{A}}^T(t_2) \\ \vdots \\ \dot{\mathbf{A}}^T(t_m) \end{bmatrix} = \begin{bmatrix} \dot{a}_1(t_1) & \dot{a}_2(t_1) & \dots & \dot{a}_n(t_1) \\ \dot{a}_1(t_2) & \dot{a}_2(t_2) & \dots & \dot{a}_n(t_2) \\ \vdots & \vdots & \ddots & \vdots \\ \dot{a}_1(t_m) & \dot{a}_2(t_m) & \dots & \dot{a}_n(t_m) \end{bmatrix} \tag{3-15}$$

Next, we built the library $\Theta(\mathbf{A})$, which is composed of nonlinear candidate functions formed from the columns of the matrix $\mathbf{A}$:

$$\Theta(\mathbf{A}) = \begin{bmatrix} | & | \\ \mathbf{A}^{P_1} & \mathbf{A}^{P_2} \\ | & | \end{bmatrix} \tag{3-16}$$

In this notation, $\mathbf{A}^{P_i}$ represents polynomial terms of order i (for instance, $\mathbf{A}^{P_2}$ corresponds to quadratic nonlinearities in the state $\mathbf{A}$). We selected a polynomial basis because, according to the N–S equations, the governing nonlinearities are exclusively quadratic.

$$\mathbf{A}^{P_2} = \begin{bmatrix} a_1(t_1) & a_2(t_1) & \cdots & a_1(t_1)a_2(t_1) & \cdots & a_1^2(t_1) & \cdots & a_n^2(t_1) \\ a_1(t_2) & a_2(t_2) & \cdots & a_1(t_2)a_2(t_2) & \cdots & a_1^2(t_2) & \cdots & a_n^2(t_2) \\ \vdots & \vdots & \ddots & \vdots & \ddots & \vdots & \ddots & \vdots \\ a_1(t_m) & a_2(t_m) & \cdots & a_1(t_m)a_2(t_m) & \cdots & a_1^2(t_m) & \cdots & a_n^2(t_m) \end{bmatrix} \tag{3-17}$$

Each column of $\Theta(\mathbf{A})$ corresponds to a candidate basis function for the right-hand side of (3-13). Since we anticipated that only a small subset of these nonlinear terms would be active in each row of $\mathbf{f}$, we formulated a sparse regression problem to compute the sparse coefficient vectors $\Xi = \begin{bmatrix} \xi_1 & \xi_2 & \cdots & \xi_n \end{bmatrix}$, thereby identifying which nonlinearities are actually present. To solve this sparsity-promoting regression, we employed Sparse Relaxed Regularized Regression (SR3). Hence, the SINDy framework can be summarized as:

$$\dot{\mathbf{A}} = \Theta(\mathbf{A})\Xi \tag{3-18}$$

Accordingly to Zheng et al. (2019) [25], SR3 is a fast and scalable method that is robust to noisy or incomplete data and sufficiently flexible to be applied widely to regularized regression problems. These include standard approaches such as LASSO and compressed sensing, composite regularizers like total variation, and even non-convex regularizers such as the $\mathcal{L}_0$ norm and

rank. Its central concept is to solve a relaxed version of the original regularized problem, which offers three main benefits: 1) the resulting solutions exhibit improved accuracy, fewer false positives, and better conditioning; 2) it enables very fast algorithms for both convex and non-convex problems; and 3) it naturally supports composite regularizers, crucial for total variation, as well as sparsity-promoting formulations based on tight frames.

Following Champion et al. (2020) [23], the SR3 framework employs relaxation and partial minimization in the form:

$$\min \frac{1}{2} \left\| \dot{X} - \Theta(X)\Xi \right\|^2 + \lambda R(W) + \frac{1}{2\nu} \|\Xi - W\|^2 \tag{3-19}$$

SR3 also permits the incorporation of symmetries and constraints into the identification procedure. This capability is particularly valuable for our methodology, as the target governing equation exhibits such type of relationships.

For the implementation, we employed the Python package of the SINDy algorithm, PySINDy [24]. As a specialized library for sparse model identification, it provides all essential tools required to apply the SINDy framework for data-driven discovery of dynamical models.

3.5 Data processing approach

For the sake of global understanding, the data-processing methodology is summarized prior to Section (4). Figure 3.5 illustrates the workflow adopted in this study to derive the reduced-order model.

First, Horna (2024) [63], conducted a dedicated data-acquisition campaign targeting the laminar separation bubble (section3.1). Owing to the adopted measurement methodology, the resulting dataset exhibits high spatial and temporal resolution. Subsequently, POD was applied to the fluctuating component of the flow field, obtained by subtracting the base flow, in order to extract the coherent flow structures and their associated temporal amplitude evolution (section 3.2). The resulting POD modes were then examined, and the most representative ones, in terms of both energetic content and spatial structure, were selected. The Galerkin projection method was employed by projecting the chosen ansatz onto the N–S equations, which yielded a system of ODEs governing the reduced-order dynamics (section 3.3).

The remaining unknown linear and bilinear coefficients of the model were identified using the SINDy algorithm (section3.4). For the optimization

within SINDy, the SR3 method was chosen, as it allows for the imposition of constraints and the enforcement of symmetries. The final outcome is a ROM that describes the transient dynamics of a LSB.

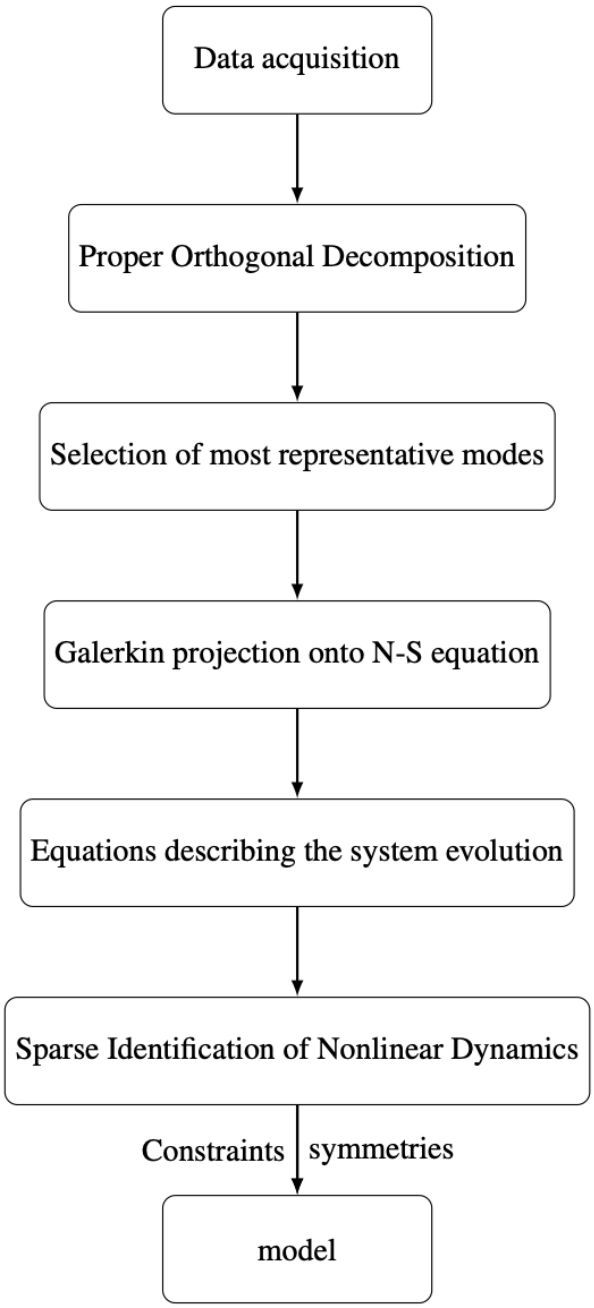

Figure 3.5: Resume of data processing methodology

4
Results

This chapter presents the results of the investigation along with their corresponding analysis and interpretation. It first addresses the qualitative characteristics of the laminar separation bubble, and subsequently examines these features using Proper Orthogonal Decomposition. Thereafter, a four-degree-of-freedom model is introduced and analyzed to describe the complete transient evolution of the system. Finally, a reduced-order model with three degrees of freedom, specifically designed to capture and characterize the vortex ejection process, is developed and discussed.

In the following discussion, several quantities are expressed in dimensionless form. The streamwise extent of the velocity field is non-dimensionalized using the streamwise coordinate of the separation point of the LSB in the quasi-steady regime, x_s, and the momentum thickness at the separation point in the quasi-steady regime, θ_s. The wall-normal extent of the velocity field is likewise non-dimensionalized with respect to the momentum thickness at the separation point of the LSB in the quasi-steady regime. The temporal coordinate is non-dimensionalized using the characteristic time scale $\tau = U_{\infty,s}/\theta_s$, where $U_{\infty,s}$ denotes the free-stream streamwise velocity at the separation of the LSB in the quasi-steady regime.

4.1
Asymptotic bubble growths

The primary objective of this section is to provide the reader with a broader perspective on the asymptotic growth of the LSB. As the scope of the present work is limited to the qualitative proposal and assessment of a ROM, an exhaustive examination of all flow characteristics and LSB features is not pursued.

In order to reveal the amount of data required for data convergence, Horna (2024) [63] analyzed the first and second statistic moments. For this purpose, the cumulative mean and cumulative standard deviation of a few representative magnitudes are evaluated and shown in Figures 4.1 to 4.5. Results suggested that 2500 samples would be the minimum amount for convergence of the selected flows statistics. However, 20 repetitions of 2500

minimum samples were collected to allow convergence for other calculations, such as for reduced order modeling.

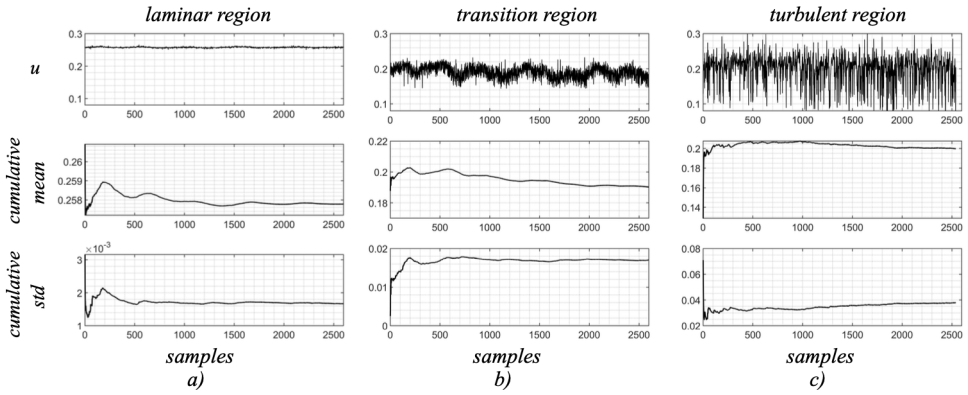

Figure 4.1: Convergence of the streamwise velocity component. a) Data convergence in the laminar part; b) Data convergence in the transient part; c) Data convergence in the turbulent part. Image extracted from Horna (2024) [63].

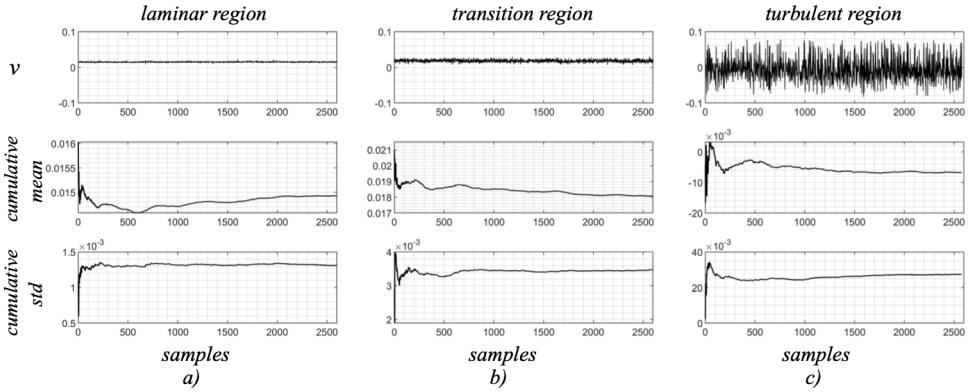

Figure 4.2: Convergence of the wall-normal velocity component. a) Data convergence in the laminar part; b) Data convergence in the transient part; c) Data convergence in the turbulent part. Image extracted from Horna (2024) [63].

The evolution of the LSB from incipient separation to a quasi-stationary state was analyzed. The corresponding transient interval is depicted in Figure 4.6. During the first 15 seconds, the bubble is fully suppressed. Over the subsequent 10 seconds, the bubble exhibits asymptotic growth until it reaches a quasi-steady regime. This behavior enables the application of an ensemble-averaging strategy with 20 realizations, with the data being phase-locked. In this manner, the asymptotic development of the bubble is characterized.

Figures 4.7 and 4.8 present snapshots of the evolution of the streamwise and wall-normal velocity components, respectively, during the transient phase of the LSB. The colorbar has maximum value of 0.3m/s and minimum of -0.3

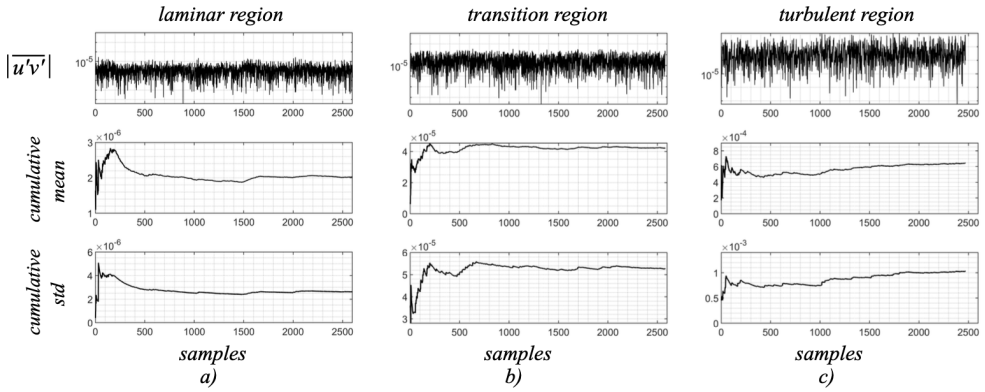

Figure 4.3: Convergence of the $|\bar{u'v'}|$ Reynolds stress component. a) Data convergence in the laminar part; b) Data convergence in the transient part; c) Data convergence in the turbulent part. Image extracted from Horna (2024) [63].

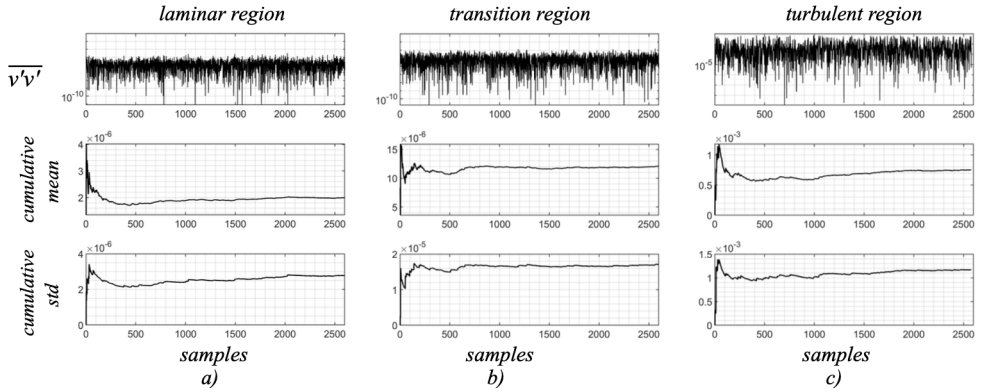

Figure 4.4: Convergence of the $|\bar{v'v'}|$ Reynolds stress component. a) Data convergence in the laminar part; b) Data convergence in the transient part; c) Data convergence in the turbulent part. Image extracted from Horna (2024) [63].

m/s. Five representative time instants were selected to discuss the underlying me chanisms governing the bubble dynamics. The instant $t/\tau = 0$ marks the onset of the transient. At this time, the bubble is completely suppressed and the boundary layer is on the verge of separating from the surface. At $t/\tau = 516$, the boundary layer remains in the process of separating. Figure 4.7 already indicates the presence of reverse flow in the streamwise direction, a hallmark of the LSB, whereas Figure 4.8 reveals no significant vortex ejection at this stage. At $t/\tau = 774$, vortex shedding becomes evident in both figures. However, subsequent time instants indicate that the bubble is still approaching its quasi-steady state. At $t/\tau = 1291$, the bubble appears to be close to its quasi-permanent regime. By $t/\tau = 1807$, the bubble has attained a quasi-steady condition. At these last two time instants, the bubble exhibits very

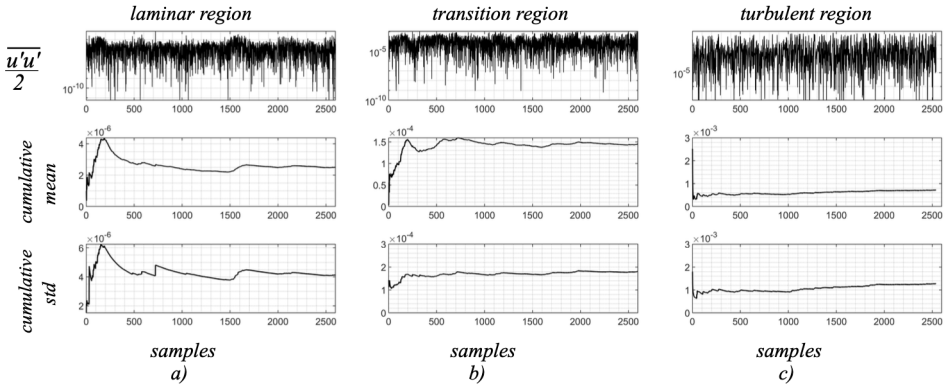

Figure 4.5: Convergence of the streamwise turbulent kinetic energy. a) Data convergence in the laminar part; b) Data convergence in the transient part; c) Data convergence in the turbulent part. Image extracted from Horna (2024) [63].

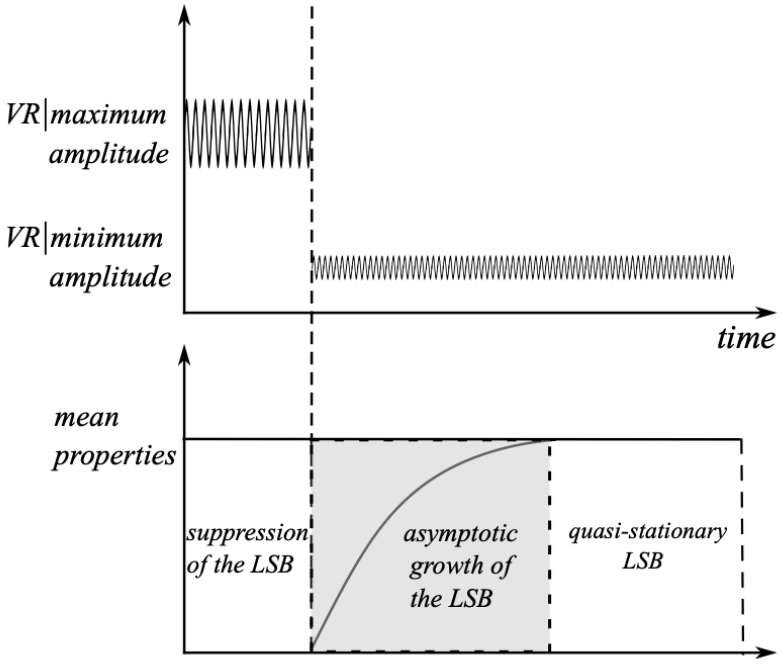

Figure 4.6: Route followed for the unforced laminar separation bubble. (Top) During the initial 15 seconds, the vibrating ribbon oscillates with high amplitude; subsequently, it is deactivated. (Bottom) The bubble is suppressed during the first 15 seconds, the next 10 seconds grows asymptotically until reaching the quasi-steady regime, then the bubble remains in its condition for 29 seconds until the end of the data recording. Image extracted from Horna (2024) [63].

similar features, such as a well-defined height, a distinct reverse-flow region, and a nearly periodic vortex-shedding pattern.

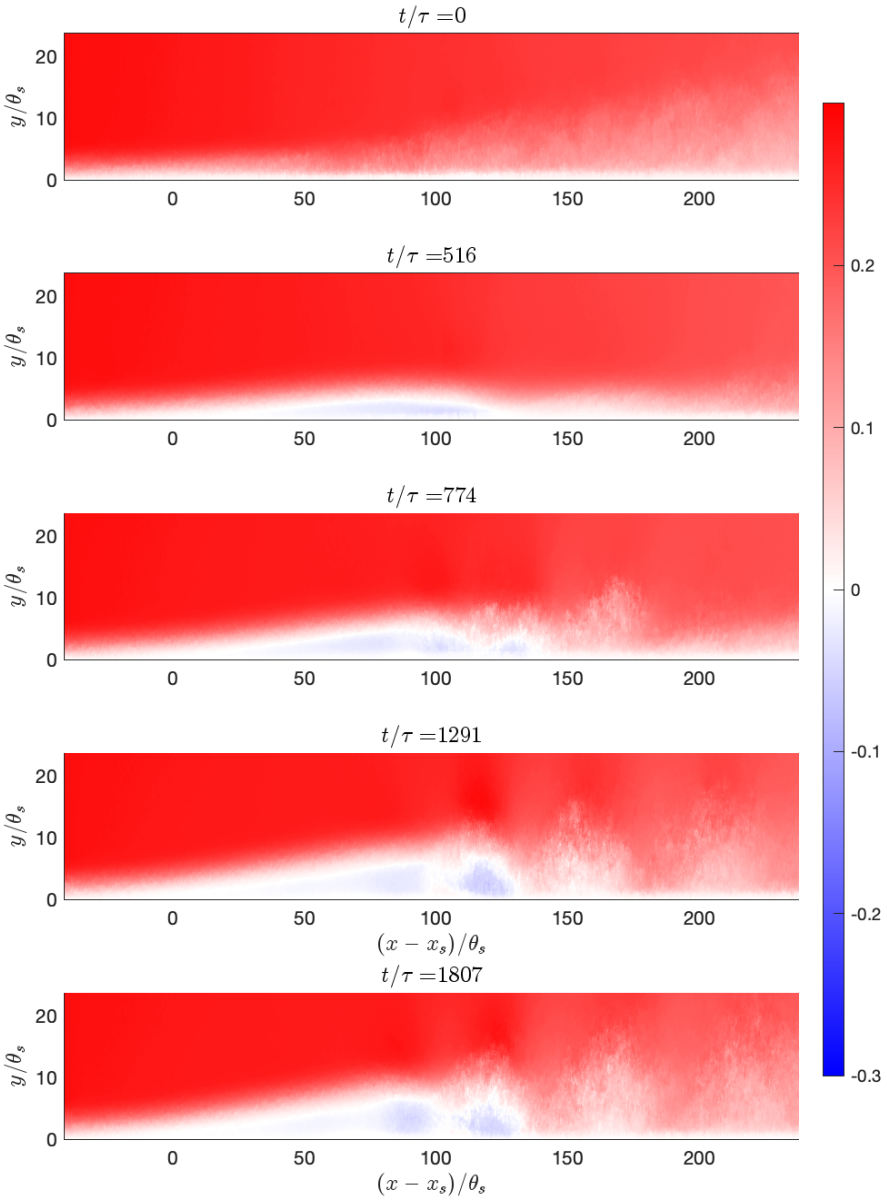

Figure 4.7: Instantaneous of the streamwise velocity during the laminar separation bubble transient growth. Colorbar is saturated with values around 0.3 m/s and represent the streamwise velocity.

4.2 Asymptotic bubble growth POD

According to Liao et al. (2023) [64], from the perspective of dynamical systems theory, the evolution of the flow can be interpreted as a transition from

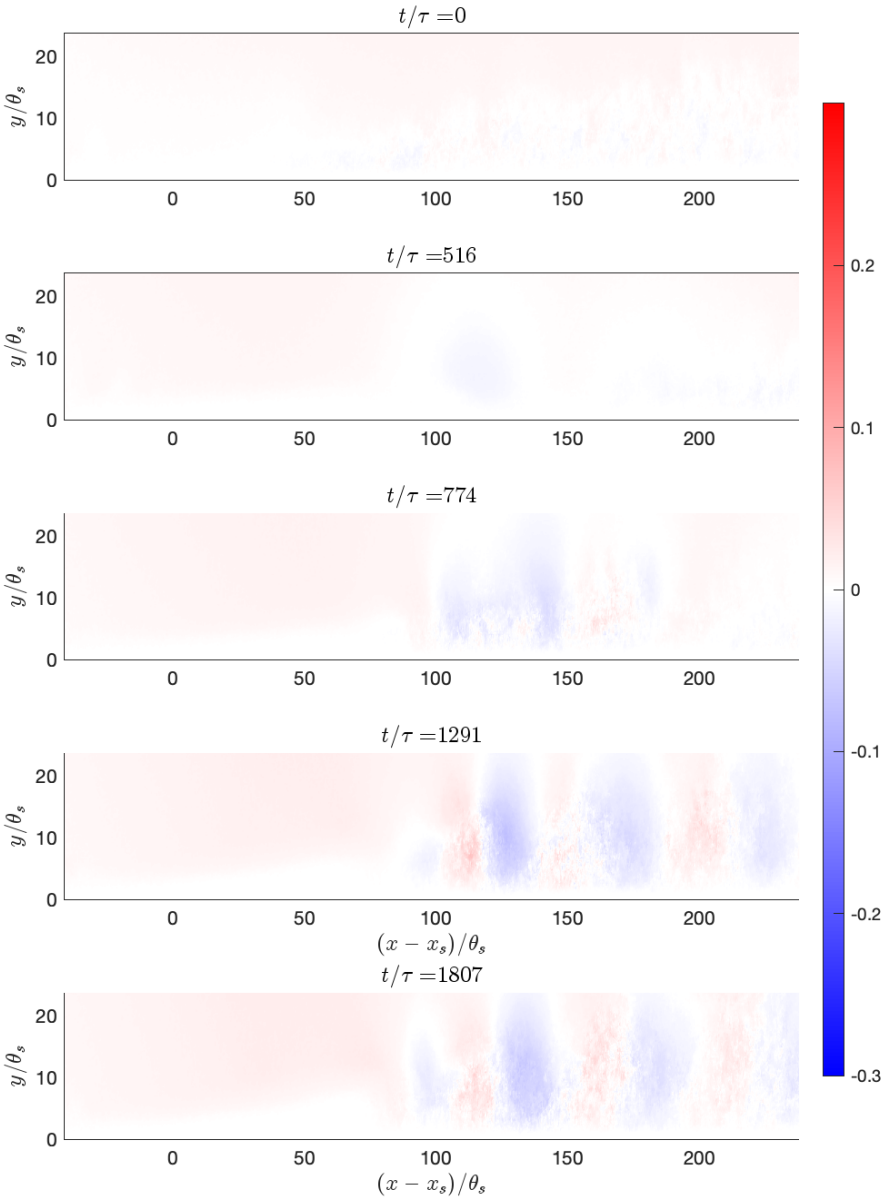

Figure 4.8: Instantaneous of the wall-normal velocity during the laminar separation bubble transient growth. Colorbar is saturated with values around 0.3 m/s and represent the wall-normal velocity.

an unstable fixed point to a stable limit-cycle oscillation. During this transition, the system sequentially traverses distinct dynamical regimes, including exponential growth, algebraic growth, and exponential relaxation. Furthermore, Sirovich (1987) [45], indicates that the dynamics evolve on a relatively

low-dimensional *strange attractor*. Modal decomposition techniques provide a powerful framework for analyzing and characterizing such behavior.

4.2.1 Obtaining the *shift mode*

To extract coherent structures and their associated temporal coefficients, we applied POD to the velocity fluctuations **u**', as defined in eq. (3-2). The data is considered only during the asymptotic growth of the LSB. This ranges from the non-separated flow to the beginning of the quasi-steady bubble regime.

Following the methodology of Noack et al. (2003) [32], the base flow state ($\bar{\mathbf{u}}(\mathbf{x})$) has to be subtracted from the data to allow the POD to capture the *shift modes*. In permanent regime cases, the base flow is similar to the mean flow most of the cases, however, as it is possible to infer from Figure 4.9, it is not the case for the LSB in the transient regime.

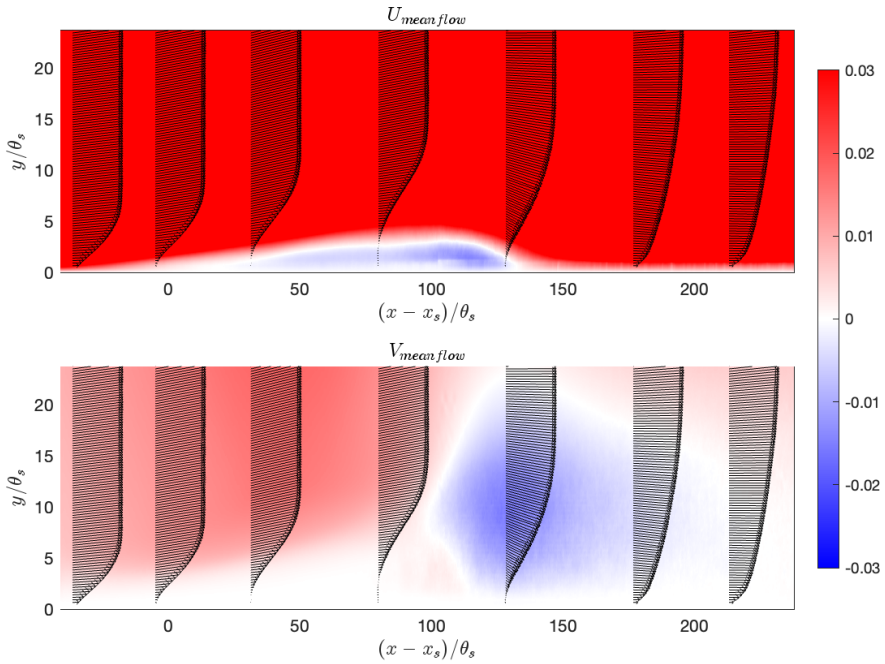

Figure 4.9: Mean flow of the laminar separation bubble during transient. (Top) Streamwise velocity. (Bottom) Wall-normal velocity. Arrows are the velocity profile at arbitrary points and the colorbar is saturated with values around 0.03 m/s and refers to both the streamwise and wall-normal velocities.

In this context, two distinct base flow states could have been selected: one corresponding to the onset of the asymptotic growth of the laminar separation bubble (see Figures 4.10), and another corresponding to its final stage (see Figures 4.11), when the boundary layer is fully separated. These two base

flows exhibit different characteristics and were obtained by ensemble averaging of instantaneous velocity fields.

The base flow at the beginning of the asymptotic growth was computed from velocity fields acquired immediately after the bubble had been fully suppressed and the amplitude of the vibrating ribbon had been reduced, and just before the bubble started to grow again. This base flow does not exhibit any indication of reverse flow in the streamwise velocity component. However, it displays a small negative wall-normal velocity, which may be attributed to the residual wake induced by the vibrating ribbon. In addition, the corresponding velocity profiles show some distortions, particularly at intermediate and downstream positions.

The base flow associated with the end of the asymptotic growth phase was obtained from velocity fields collected after the bubble had reached its quasi-steady state, up to the end of the recording. Consequently, this flow represents the LSB in a statistically quasi-steady regime. In this case, the streamwise velocity clearly exhibits reverse flow and the typical features of a recirculating separation bubble. The evolution of the velocity profiles, as depicted in the figure, clearly shows the presence of reverse flow.

For the subsequent analyses, the base flow at the beginning of the asymptotic growth was selected, owing to its more homogeneous and not separated character compared with the alternative base flow state.

4.2.2 Proper Orthogonal Decomposition

The proper orthogonal decomposition of ensemble averaged velocity fields is performed according to the methodology described in Section 3.2. The Figure 4.12 shows the cumulative energy of all POD modes. According to the figure, 41% of the flow energy during bubble formation is contained in the first 15 modes. The figure shows that some modes appear in pairs, whereas others do not. The pairs represent oscillatory modes, and the other are related to transient or non-converged modes. According to the energy rank, the two most energetic modes are transient, and the third and fourth are oscillatory.

The POD modes are presented in Figures 4.13 and 4.14. The horizontal axis represents the dimensionless length and the vertical axis the dimensionless height. Both coordinates are nondimensionalized by the momentum thickness at the separation point of the bubble in the quasi-steady state, and the length is shifted by the separation position. It is important to emphasize that, by construction, it is reasonable to assume that each eigenfunction is incompressible and satisfies the boundary conditions of the problem, since each

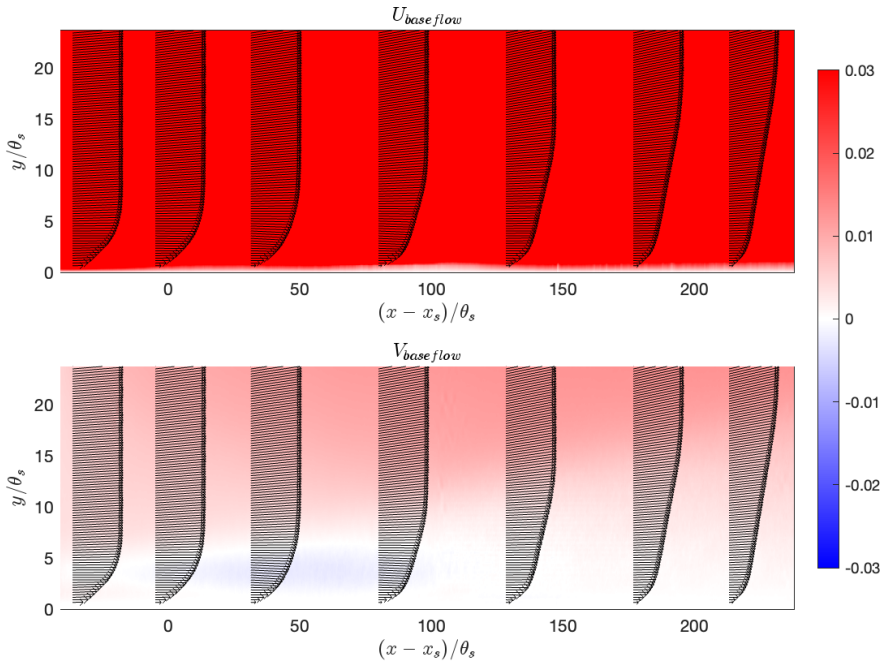

Figure 4.10: Base flow at the beginning of the asymptotic growth. (Top) Streamwise velocity. (Bottom) Wall-normal velocity. Arrows are the velocity profile at arbitrary points and the colorbar is saturated with values around 0.03 m/s and refers to both the streamwise and wall-normal velocities.

eigenfunction is formed as a superposition of instantaneous flow fields [45]. The modes are organized hierarchically, with the most energetic mode located in the top-left position and the least energetic mode in the bottom-right position. The corresponding temporal coefficients are shown in Figure 4.15.

The amplitude evolution of modes shown in Figure 4.15 indicates that modes 1 and 2 vary during the initial stage of the transient until they reach a quasi-steady behavior. Mode 2 initially dominates the dynamics, and once its amplitude reaches a maximum near the nondimensional time 750, mode 1 becomes the dominant contributor. At approximately the same time, the oscillatory modes exhibit an increase in growth rate, suggesting an intimate coupling with mode 1. Modes 5 and 6 are also non-oscillatory, but with considerably less energy than modes 1 and 2. Modes 1, 2, 5 and 6 are low-frequency and are associated with the low-frequency dynamics of the separation bubble. Modes 1 and 2 play a leading role on the bubble formation, and modes 5 and 6 seems to be related to higher order effects. The remaining modes appear to correspond to higher harmonics of modes 3 and 4.

Examination of the spatial structures associated with the modes shows that they exhibit strong coherence in the beginning of the streamwise direction,

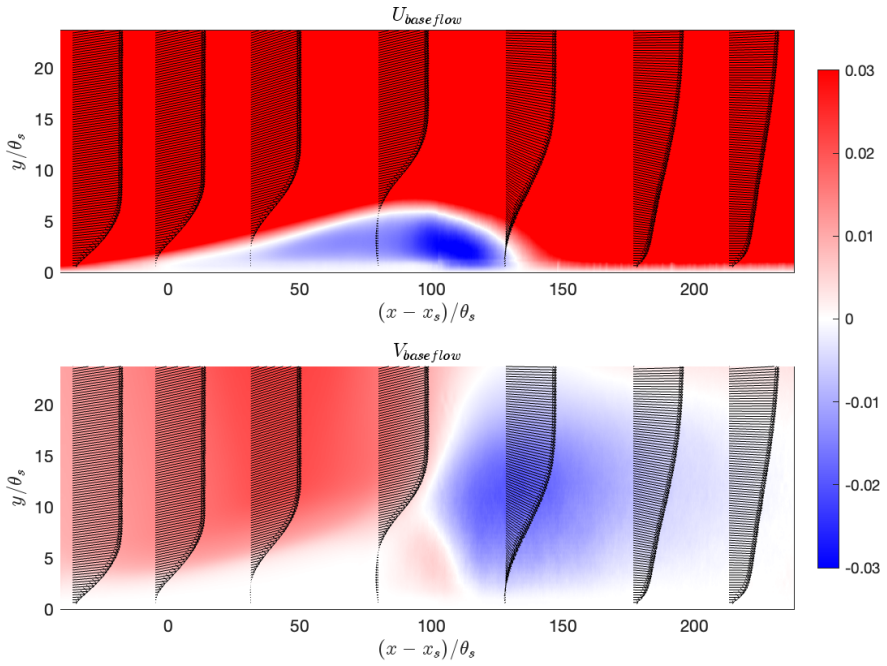

Figure 4.11: Base flow at the end of the asymptotic growth. (Top) Streamwise velocity. (Bottom) Wall-normal velocity. Arrows are the velocity profile at arbitrary points and the colorbar is saturated with values around 0.03 m/s and refers to both the streamwise and wall-normal velocities.

however this coherence progressively deteriorates. The wall-normal modes exhibit a characteristic pattern of oscillatory components, with a clear harmonic structure. Because the dominant element in the flow velocity is aligned with the streamwise direction, most coherent structures of the low frequency modes are less energetic in wall normal velocity component than in streamwise one. Streamwise modes 1 and 2 capture the boundary-layer separation and the recirculating region. Modes 5 and 6 also represent part of this dynamics, although with significantly lower energy content. Consequently, modes 1 and 2 are dominant and captures the principal features of the system. Modes 3 and 4 represent the Kelvin-Helmholtz instability. The other oscillatory modes also characterize this instability, but at smaller spatial and energetic scale. The oscillatory modes are responsible for the vortex-shedding dynamics of the separation bubble, with the largest associated energy contained in modes 3 and 4. These findings are in good agreement with the results reported by Michelis et al. (2017) [19].

To explore the state space and gain further insights into the dynamics, curves $a_1 \times a_{3,4}$ and $a_2 \times a_{3,4}$ (Figures 4.16) were constructed. These curves represent trajectories associated with the transient laminar separation bubble

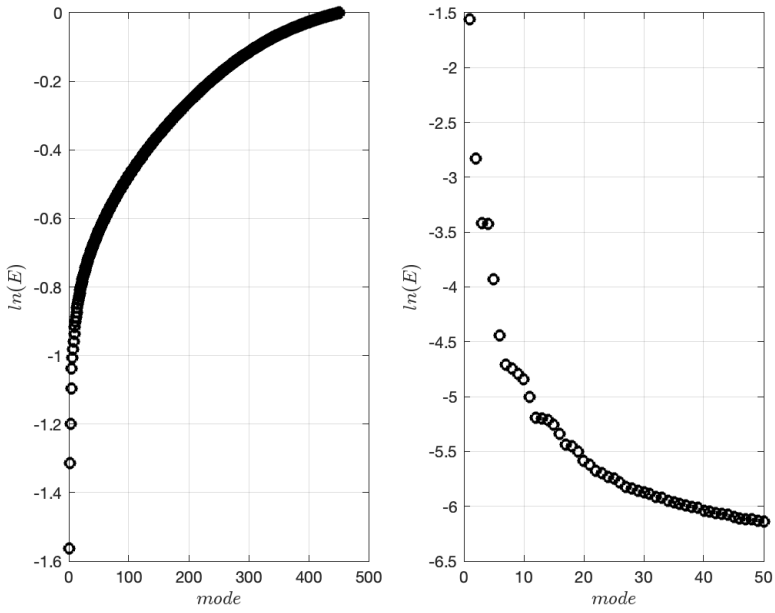

Figure 4.12: Energy plot of POD modes in logarithmic scale. (Left) Cumulative energy of all 450 obtained modes. (Right) Energy of each mode for the first 50 modes.

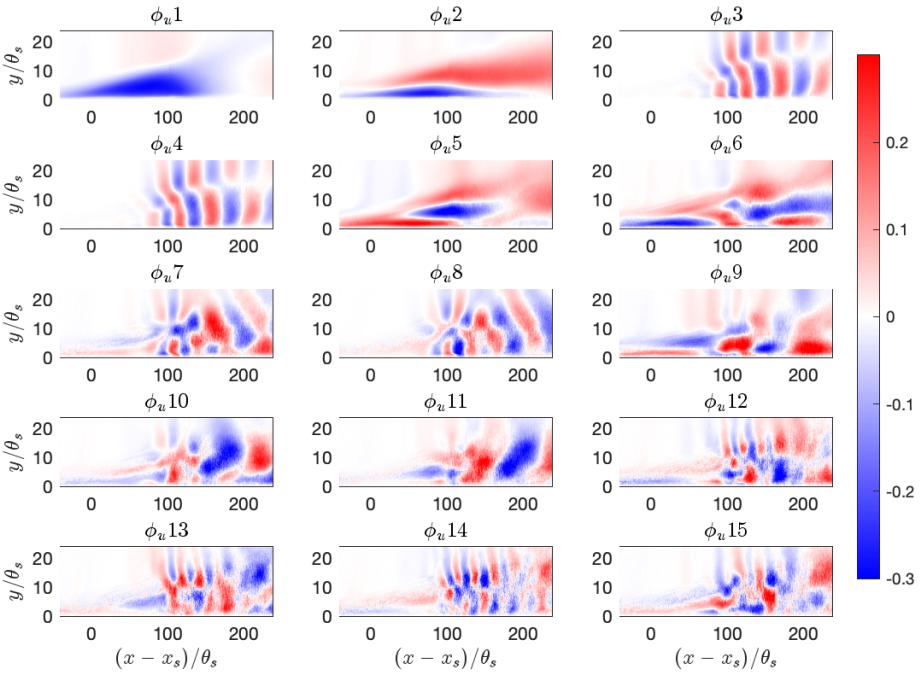

Figure 4.13: Streamwise velocity POD modes. Colorbar is saturated with values around 0.3 m/s and represent the streamwise velocity.

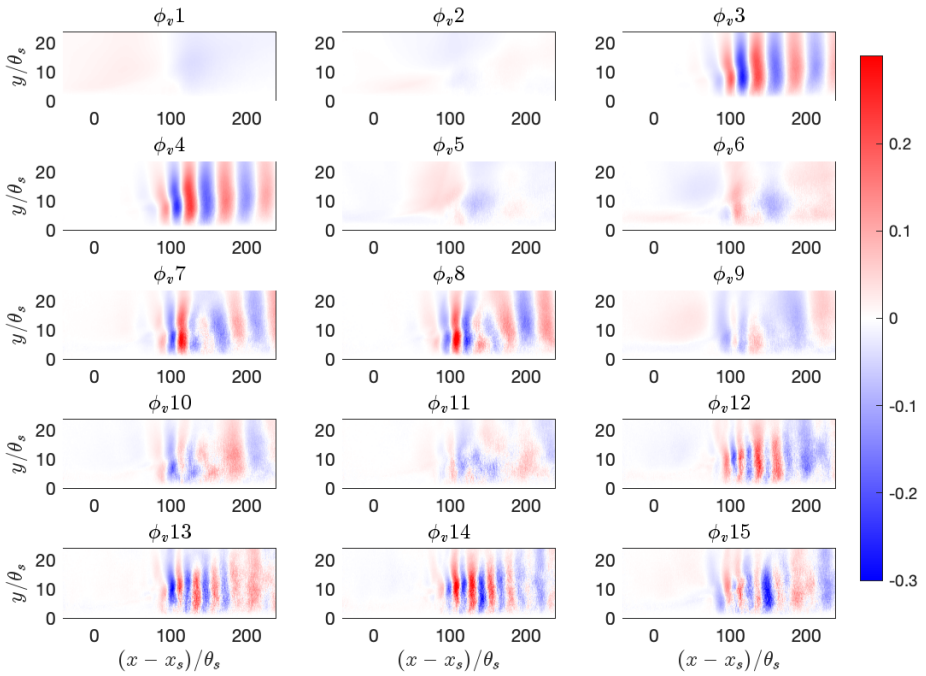

Figure 4.14: Wall-normal velocity POD modes. Colorbar is saturated with values around 0.3 m/s and represent the wall-normal velocity.

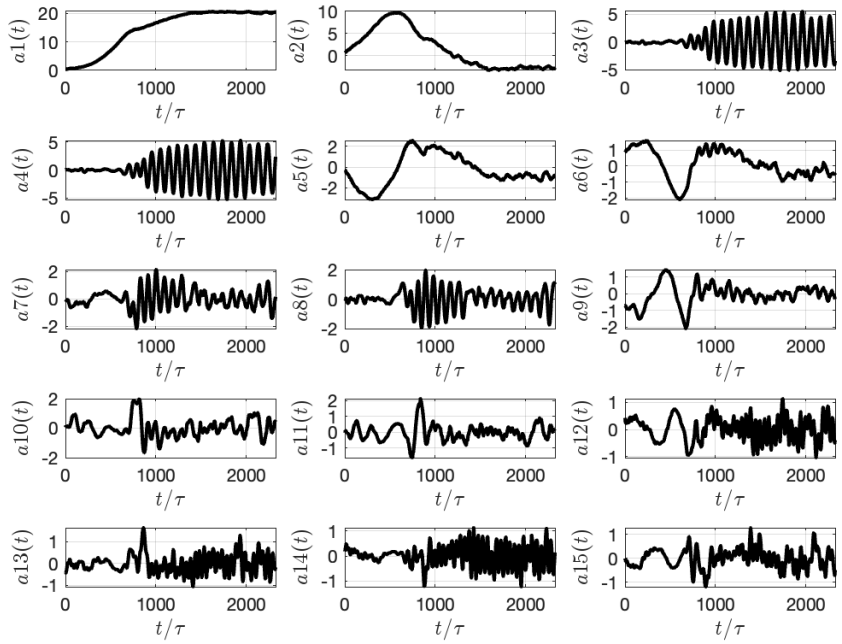

Figure 4.15: Amplitude evolution POD modes

and exhibit distinct evolutionary characteristics. This behavior different from what is commonly reported in the literature for fluid flows [32, 35], where it is unusual to observe two distinct modes modulating the invariant manifold. The present result suggests that the system dynamics evolve from two different regions in state space, implying the existence of more than one unstable equilibrium (or fixed) point from which the trajectories originate. It further indicates that modes 1 and 2, together with modes 3 and 4, are essential for accurately characterize the global flow dynamics and, therefore, have a significant impact in the predictive capability of the derived low-dimensional model.

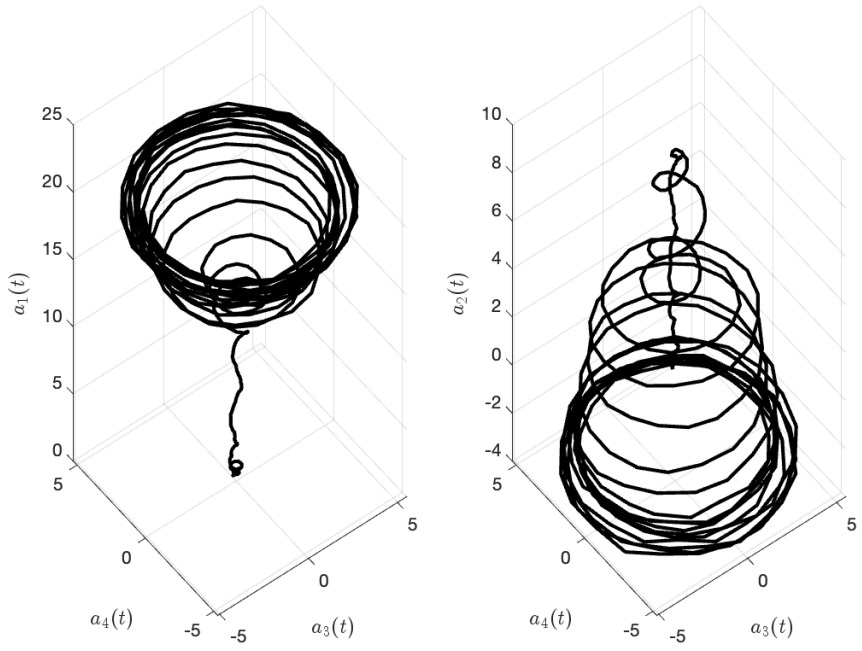

Figure 4.16: State space evolution of the transient laminar separation bubble.

4.3 Manifold investigation

A peak in the temporal coefficient of the second mode indicates that, from that instant onward, the system evolves on a different invariant manifold. To verify this interpretation, the vorticity transport equation (4-1) was employed to determine the time instant that could correspond to a steady-state solution ($\partial w/\partial t = 0$).

$$\frac{\partial w}{\partial t} + u\frac{\partial w}{\partial x} + v\frac{\partial w}{\partial y} - \frac{1}{Re}(\nabla^2 w) = 0 \tag{4-1}$$

Where u and v denote the streamwise and wall-normal velocity components, respectively, $w = \nabla \times (u, v)$ is the vorticity, $\nabla^2 = (\partial^2/\partial x^2 + \partial^2/\partial y^2)$ is the Laplacian operator.

The experimental data was employed to estimate the residuals of the transport equation. Residuals were calculated for each measured time instant and averaged over short intervals to reduce noise due to derivatives of experimental data. According to this analysis, the configuration exhibiting the lowest residual (Figure: 4.18) was for the averaged $t_0 = 895$ and $t_f = 905$, which corresponds to the peak at the amplitude evolution of the second mode. Interpretation remained challenging due to the inherent noise in experimental measurements. Nevertheless, by analyzing the vorticity transport formulation of the N–S equations at this optimal time (Figure 4.17), the presence of an additional steady point in the dynamical system can be confirmed.

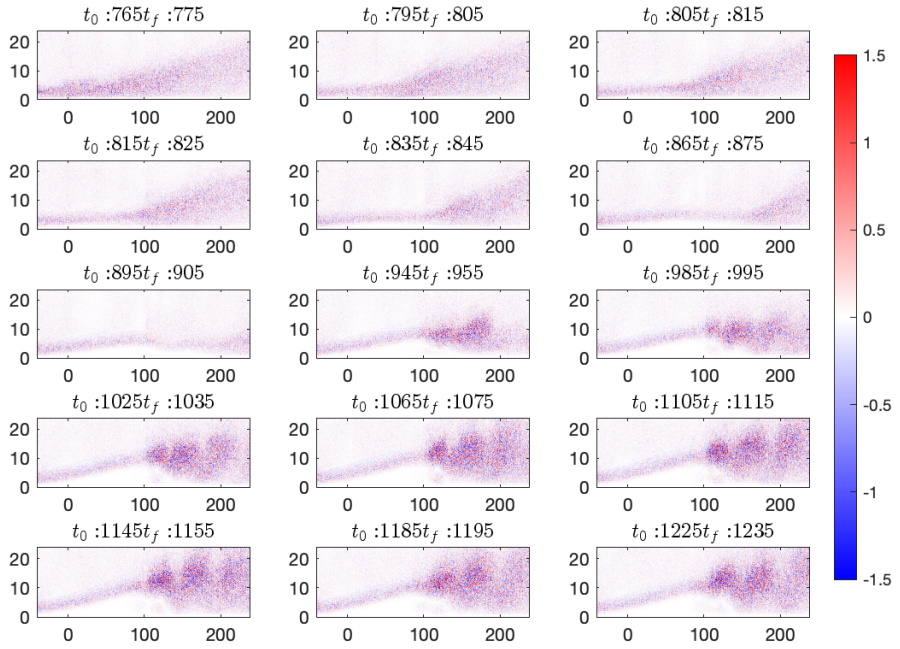

Figure 4.17: Residuals of the streamwise velocity POD modes

The results in Figure 4.17 suggests that the evolution from unstable state 1, at the initial time of the transient, to unstable state 2 is associated with boundary-layer separation and subsequent reattachment, leading to the formation of the separation bubble. Next, the evolution from state 2 appears to be governed by vortex-shedding dynamics, similarly to those observed in the wake of bluff bodies.

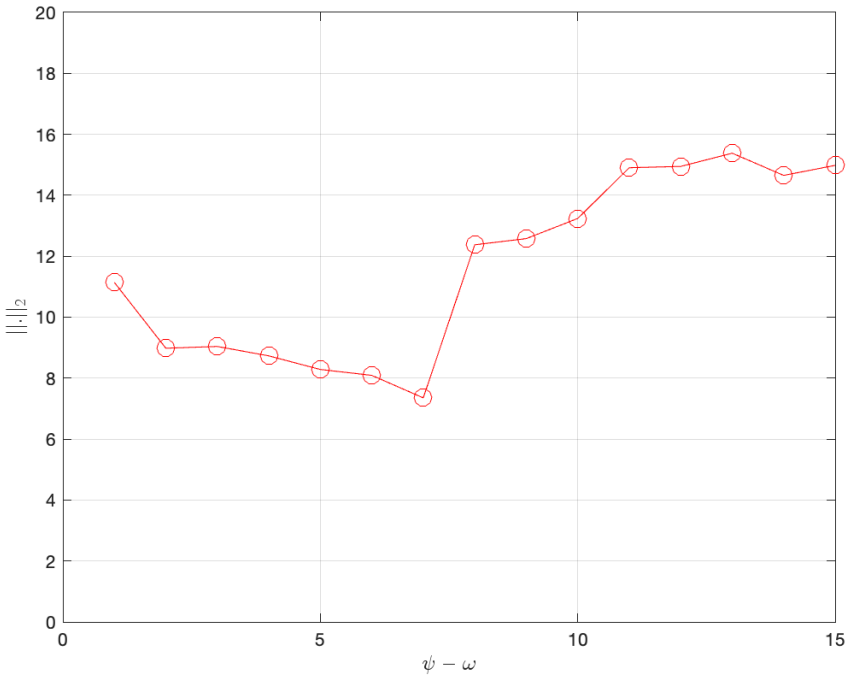

Figure 4.18: Cumulative residual of each flow field

In the horizontal axis of the residual plot (Figure 4.18) the different flow fields are represented, whereas the vertical axis corresponds to the $\mathcal{L}_2$ norm employed to quantify the discrepancy between them. The results indicates that the initial stage of the transient has already evolved in time. The result may be mistaken due to the characteristics of the experiment (i.e. the passing wake to suppress the bubble). The scenario that has the smallest residual is the one that matches the peak of the second mode. This observation is consistent with the hypothesis that the underlying manifold evolves from two distinct unstable equilibrium states, and that two static modes are required to represent the changes between the base flow and the quasi-steady regime.

In the following, we introduce a new four-degrees-of-freedom POD-Galerkin model capable of reproducing the complete transient dynamics of the LSB, together with a standard three-degrees-of-freedom POD-Galerkin for the final instants of the transient dynamics.

4.4 Four degrees of freedom model

The objective of the present work is therefore to construct a physically interpretable model that accurately reproduces the complete dynamical behavior of the LSB. To this end, the POD-Galerkin is a natural candidate for

the development of a reduced order model. The POD analysis of the flow field indicates that the first four modes captures the most relevant characteristics of the separation bubble, and are thus essential to represent the dynamics in a model.

The spatial structure and temporal evolution of the modes selected to build the model are shown in Figure 4.19. The first and second modes describe the large-scale topological changes of the bubble and can be interpreted, following Noack et al. (2003) [32], as corrections of the mean flow. These modes are essential to represent the transient dynamic behavior. The third and fourth modes are associated with vortex shedding, which is an important component in the bubble dynamics, as already discussed in the literature review

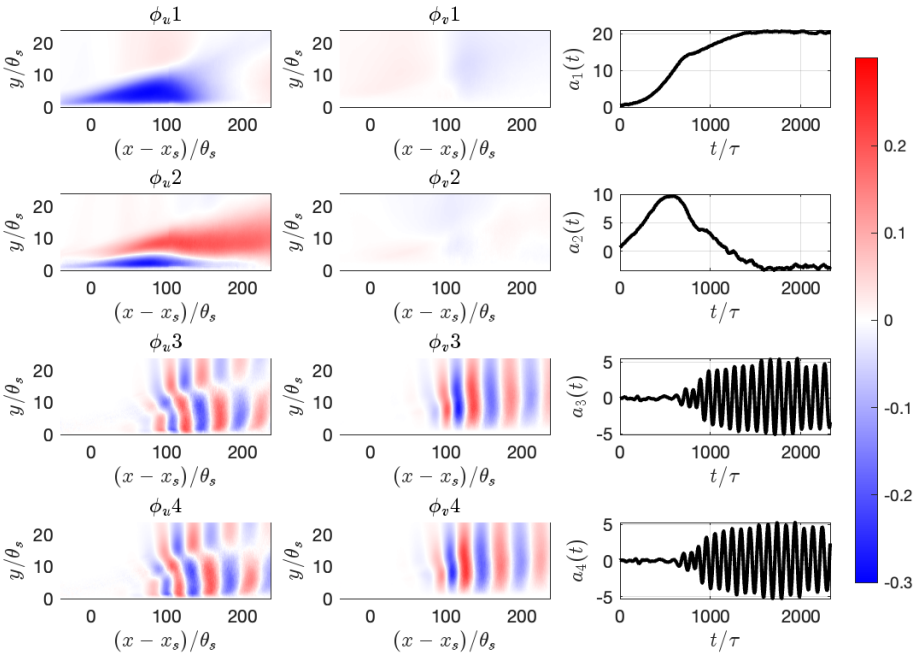

Figure 4.19: Modes used in the POD-Galerkin model and amplitude evolution

Thus, the ansatz for the reduced flow is given by eq. 4-2. where $\mathbf{u}_s(\mathbf{x})$ is the base flow (Figure 4.10) and $a_i(t)\mathbf{u}_i(\mathbf{x})$, for $i = 1, .., 4$ are the time amplitude and POD modes.

$$\mathbf{u}(\mathbf{x}, t) \approx \mathbf{u}_s(\mathbf{x}) + a_1(t)\mathbf{u}_1(\mathbf{x}) - a_2(t)\mathbf{u}_2(\mathbf{x}) + a_3(t)\mathbf{u}_3(\mathbf{x}) + a_4(t)\mathbf{u}_4(\mathbf{x}) \quad (4\text{-}2)$$

Usually, the *shift-mode* modulates the amplitude of the oscillatory dynamics. In the present study, this meanfield correction is represented through the coupling between modes 1 and 2. The combination that best approximate

the modulation of the oscillation is given by $a_1 - a_2$, as illustrated in Figure 4.20. This is not a common outcome in the literature, where the meanfield correction is usually associated with a single mode; however, the presence of two modes fulfilling this role is essential in order to obtain a meaningful ROM for the bubble. By substituting the ansatz (4-2) into the galerkin projection of the N-S equation defined in (3-5), we can retrieve the POD-Galerkin model as a linear-quadratic system of ODEs (4-3). The derivation of the model is in the Appendix A.

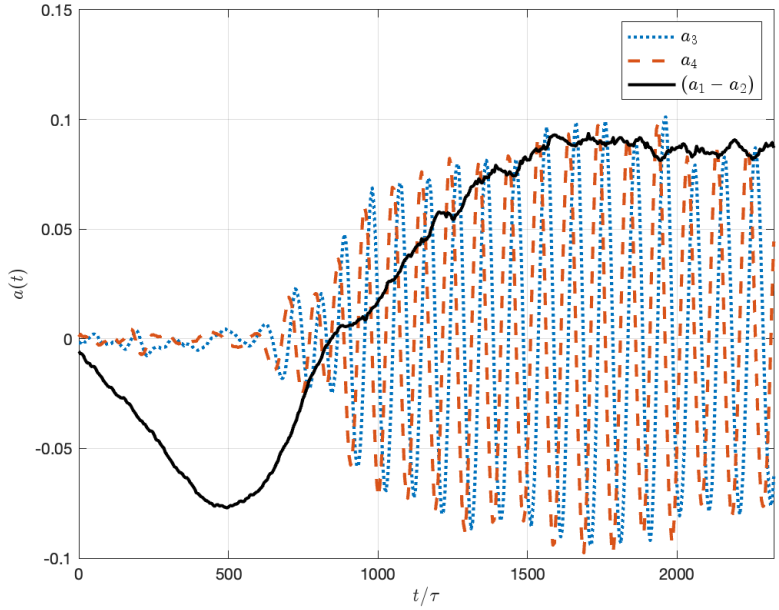

Figure 4.20: $a_1 - a_2$ plotted against a_3 and a_4.

$$\dot{a}_1 = \sigma_1 a_1 - \zeta_1 a_1 a_2 + \beta_1(a_3^2 + a_4^2) - \gamma_1 a_1^2 \tag{4-3}$$

$$\dot{a}_2 = \sigma_2 a_2 - \zeta_2 a_1 a_2 - \beta_2(a_3^2 + a_4^2) - \gamma_2 a_2^2 \tag{4-4}$$

$$\dot{a}_3 = \sigma a_3 - \omega a_4, \qquad \sigma = \sigma_3 - \beta_3 a_1 + \beta_4 a_2 \tag{4-5}$$

$$\dot{a}_4 = \omega a_3 + \sigma a_4, \qquad \omega = \omega_3 - \gamma_3 a_1 - \gamma_4 a_2 \tag{4-6}$$

The resulting model exhibits several symmetries that arise from its intrinsic properties. The first two equations describe the temporal evolution of the first two modes, both of which correspond to corrections to the mean field. It is noteworthy that a nonlinear coefficient appears, indicating a coupling relation between these two modes.This is an unusual result in the literature. Moreover, the two equations share a similar algebraic structure. The last two equations govern the dynamics of the oscillatory modes. These equations are

analogous due to the inherent pairing between the corresponding modes. In this formulation, σ_i denotes the growth rate, ω the oscillation frequency, and ζ_i, β_i, and γ_i are nonlinear coefficients.

With the algebraic form of the model specified, it remained to determine all unknown coefficients. To this end, we employed the SINDy algorithm [22, 24]. Manually imposing the symmetries, and using as training data the temporal evolution of the most dynamically relevant features, the algorithm exploits sparse regression to find all coefficients. Because the dynamics evolves on a four-dimensional, complex manifold, it was necessary to constraint the growth rate associated to a_2 as well as the nonlinear coefficients β_4 and γ_4 to ensure consistency with the reference data. The resulting identified POD-Galerkin model is given in (4-7).

$$\dot{a}_1 = 2.051a_1 - 0.029a_1a_2 + 0.105(a_3^2 + a_4^2) - 0.110a_1^2 \tag{4-7}$$

$$\dot{a}_2 = 2.300a_2 - 0.170a_1a_2 - 0.120(a_3^2 + a_4^2) - 0.097a_2^2 \tag{4-8}$$

$$\dot{a}_3 = \sigma a_3 - \omega a_4, \qquad \sigma = 0.398 - 0.007a_1 + 0.110a_2 \tag{4-9}$$

$$\dot{a}_4 = \omega a_3 + \sigma a_4, \qquad \omega = -1.140 - 0.840a_1 - 0.800a_2 \tag{4-10}$$

An examination of the model coefficients reveals several notable features. First, all four modes are linearly unstable, which is not an typical behavior in linear-quadratic low-order models in fluid mechanics, such as those proposed by Noack et al. (2003) [32], Loiseau and Brunton (2018) [39], and Deng et al. (2020) [35]. In such models, usually there is a slaved *shift mode*. The present model indicates that modes 1 and 2 are non-oscillatory (static) modes, whereas modes 3 and 4 together constitute a single complex oscillatory mode, characterized by the complex amplitude $A = a_3 + ia_4 \in \mathbb{C}$. The two static modes possess linear growth rates approximately five times larger than that of the oscillatory mode. Modes 1 and 2 are self-saturating, as evidenced by the negative sign of the quadratic self-interaction terms in Equations. (4-7) (4-8). The complex oscillatory mode is nonlinearly saturated by mode 1, while it amplifies mode 2. The squared modulus $|A|^2$ of the oscillatory amplitude enhances the effective linear instability of mode 1 and, conversely, saturates that of mode 2. Furthermore, mode 1 saturates the linear instability of mode 2, whereas mode 2 amplifies that of mode 1. The resulting network of modal interactions is summarized schematically in Figure 4.21.

The comparison between the model prediction and the data amplitude evolution is presented in Figure 4.22. The ROM accurately reproduces the trajectory of the system on the underlying manifold, reproducing the predominant dynamical features of the flow in both the transient and quasi-steady regimes.

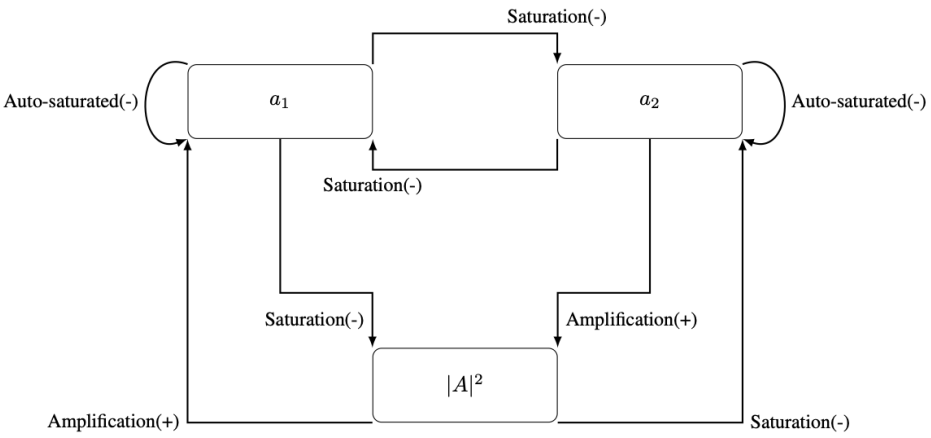

Figure 4.21: Four degree of freedom interpretation.

The first and second mode growth rate and amplitude in the limit cycle are correctly capture, although the second mode displays a small difference at its optimal time. The oscillatory modes show an excellent agreements in both the growth rate and frequency with the reference data. Furthermore, finer details of the dynamics, such as the amplitude overshoot following the initial growth phase, are also well captured.

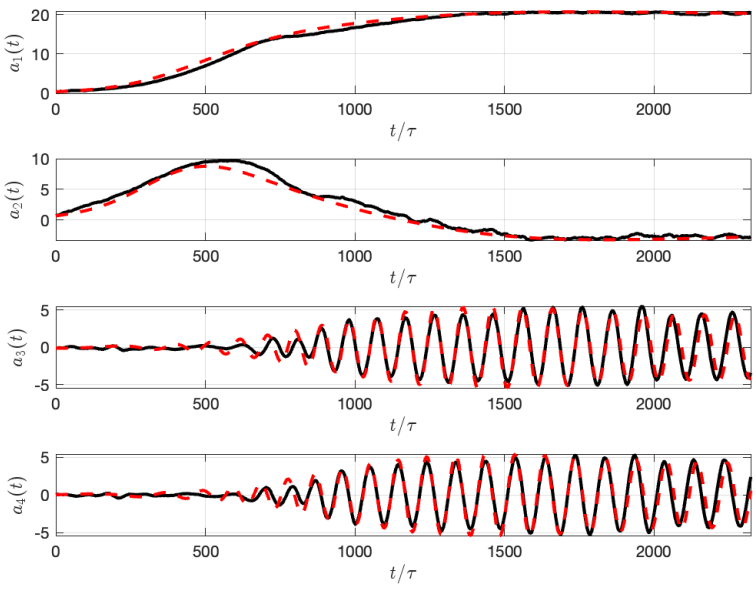

Figure 4.22: Comparison between ROM amplitude evolution (red dashed line) and real data (full black line)

Although all four modes exhibit positive linear growth rates, the initial phase of the transient bubble growth dynamics indicates that the base flow is

primarily unstable with respect to the first two static modes. The oscillatory mode requires mode 2 to attain a sufficiently large amplitude, relative to that of mode 1, before it can be effectively excited and start to grow. Moreover, it does so with a substantially smaller linear growth rate than the two static modes. As mode 2 transfers energy to the other active modes, its amplitude first increases to a maximum and subsequently decreases, ultimately saturating at a non-zero asymptotic level once the recipient modes have reached their respective saturation amplitudes.

The ROM provides physical insights about relation between modes. It is challenging to attribute a more specific physical meaning to the individual modes beyond the observation that they represent together the meanfield deformation between the base flow and the steady state. Consequently, they capture all features that characterize the mean LSB. In counter part, the oscillatory modes are associated with the K-H instability and the vortex shedding dynamics. This result is broadly consistent with literature.

4.5 Three degrees of freedom model

As evidenced by the previous results obtained from the POD analysis and the vorticity transport results, the dynamical system also evolves from an unstable point at a dimensionless time of approximately $time = 515$. To investigate this behavior, we employed the same methodology as for the previous model. First, we recomputed the POD from the optimal time up to the quasi-steady regime in order to obtain the coherent structures and their corresponding temporal amplitude evolutions. Based on the modal energy content and its spatial characteristics, we selected the most representative modes for describing the system dynamics. These modes were subsequently projected onto the governing equations to construct the POD-Galerkin model. The SINDy algorithm is then applied to identify the associated model coefficients.

The first fifty modes are presented in Figure 4.24 and 4.25. Notably, in contrast to the previous model, there is now only one static mode with significant energy content (Figure 4.23). This mode correspond to the *shift mode* which represents the meanflow deformation, in agreement with the findings of Noack et al. (2003) [32]. K-H like structures appear in the decomposition as oscillatory modes 2 and 3. The fourth mode is also a static mode, but its contribution to the dynamics most relevant features is negligible, as indicated by its relatively low energy. The remaining modes are oscillatory and represent higher harmonics of modes 2 and 3. The corresponding temporal evolution is displayed in Figure 4.26.

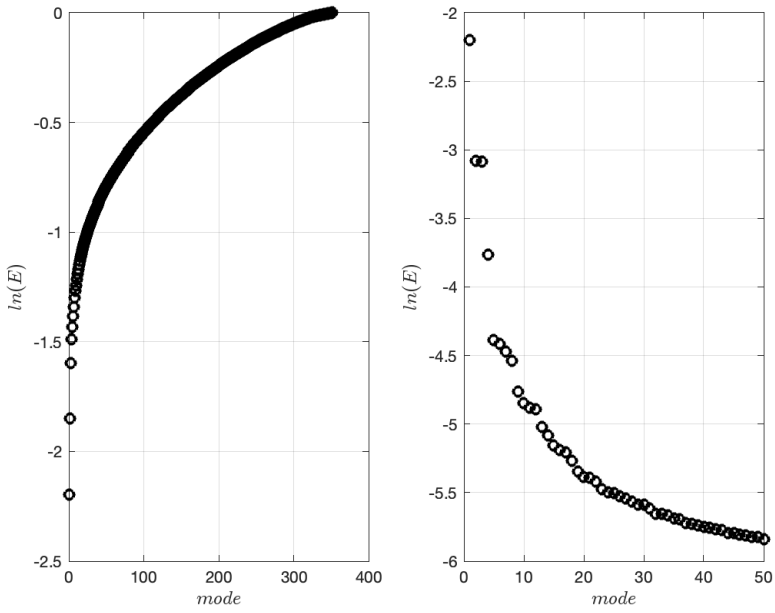

Figure 4.23: Energy plot of POD modes in logarithmic scale. (Left) Cumulative energy of all 350 obtained modes. (Right) Energy of each mode for the first 50 modes.

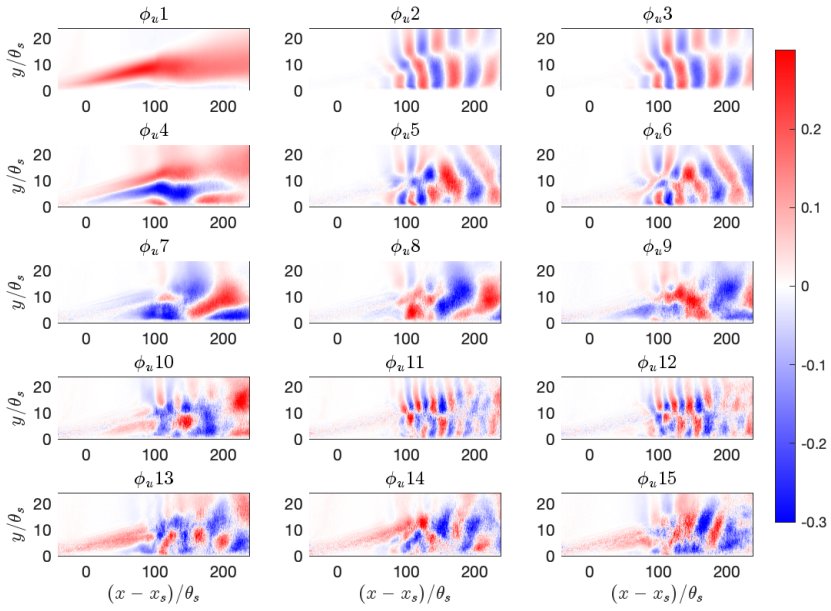

Figure 4.24: Streamwise velocity POD modes. Colorbar is saturated with values around 0.3 m/s and represent the streamwise velocity.

For the POD-Galerkin model, the asnatz (4-11) was employed, where $\mathbf{u}_s(\mathbf{x})$ denotes the same base flow as in the previous model (4.10) and $a_i(t)\mathbf{u}_i(\mathbf{x})$,

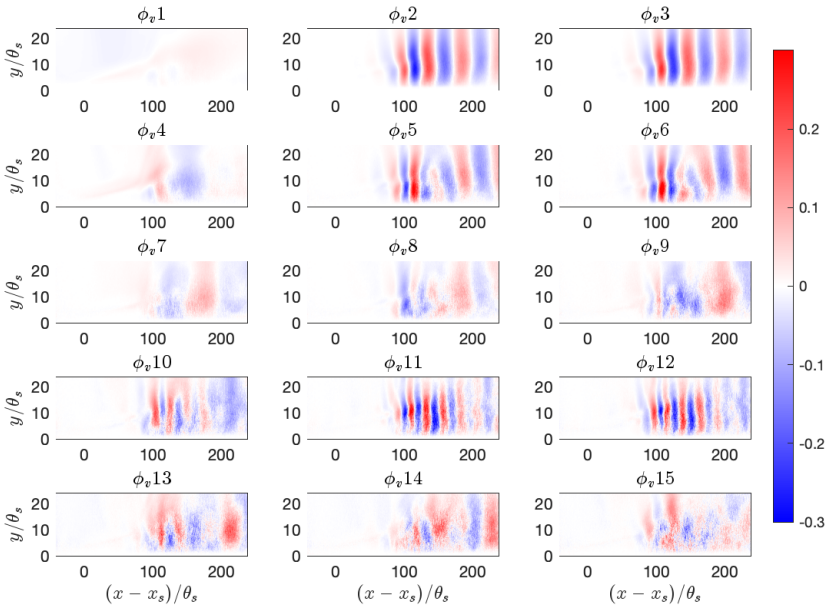

Figure 4.25: Wall-normal velocity POD modes. Colorbar is saturated with values around 0.3 m/s and represent the wall-normal velocity.

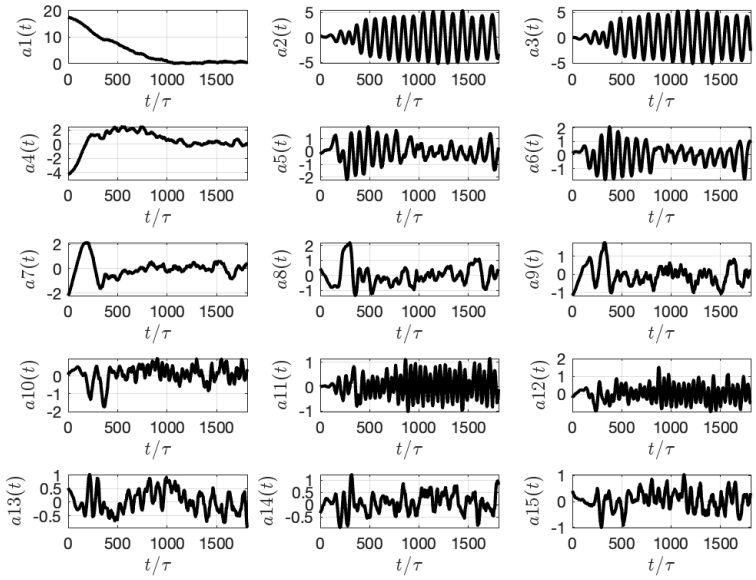

Figure 4.26: Amplitude evolution POD modes

for $i = 1, .., 3$, are the amplitude evolution times of the POD mode. The resulting model is given by equation (4-12). In this case, the POD yields one steady mode and two oscillatory modes.

$$\mathbf{u}(\mathbf{x},t) \approx \mathbf{u}_s(\mathbf{x}) + a_1(t)\mathbf{u}_1(\mathbf{x}) + a_2(t)\mathbf{u}_2(\mathbf{x}) + a_3(t)\mathbf{u}_3(\mathbf{x}) \tag{4-11}$$

$$\begin{aligned}
\dot{a}_1 &= \sigma_1 a_1 + \beta_1(a_2^2 + a_3^2) && (4\text{-}12)\\
\dot{a}_2 &= \sigma a_2 - \omega a_3, \qquad \sigma = \sigma_2 + \beta_2 a_1 && (4\text{-}13)\\
\dot{a}_3 &= \omega a_2 + \sigma a_3, \qquad \omega = \omega_2 + \gamma_2 a_1 && (4\text{-}14)
\end{aligned}$$

The resulting reduced-order representation is yields the Landau equation with cubic damping term [35], thereby providing strong evidence that the system's dynamics are governed by a supercritical Hopf bifurcation. This, in turn, implies that the instability arises through a pair of oscillatory modes.

As outlined in section 3.4, the coefficients of the POD-Galerkin system were identified using a sparse regression algorithm. Within this procedure, the nonlinear coefficients β_2 and γ_2 were adjusted to ensure agreement with the reference data. Although symmetries were imposed, no additional constraints on the remaining coefficients were required, and the algorithm correctly predict their values. In this fashion, a three-dimensional ROM was obtained, constructed from the first three POD modes. The application of sparse regression within the SINDy framework yields:

$$\begin{aligned}
\dot{a}_1 &= -0.435a_1 - 0.026(a_2^2 + a_3^2) && (4\text{-}15)\\
\dot{a}_2 &= \sigma a_2 - \omega a_3, \qquad \sigma = -0.092 + 0.095a_1 && (4\text{-}16)\\
\dot{a}_3 &= \omega a_2 + \sigma a_3, \qquad \omega = 16.184 + 0.120a_1 && (4\text{-}17)
\end{aligned}$$

The model identifies a slaved *shift mode* and a pair of complex oscillatory modes, parametrized by the complex amplitude $A = a_3 + ia_4 \in \mathbb{C}$. This outcome is consistent with previous literature of ROMs for fluid flows. The growth rate of the slave mode is 4.7 times larger than that of the oscillatory mode, thereby ensuring the slave relationship between these modes. A comparison between reference data and the ROM is presented in Figures 4.27. As anticipated, the ROM reproduces the essential dynamical features of the system. The first mode exhibit a smaller linear growth rate than observed in the reference data, which manifests as a slight delay in the linear growth of the oscillatory modes. Nevertheless, the ROM shows good agreement with the reference data and can reproduce the vortex shedding dynamics and low-frequency behavior.

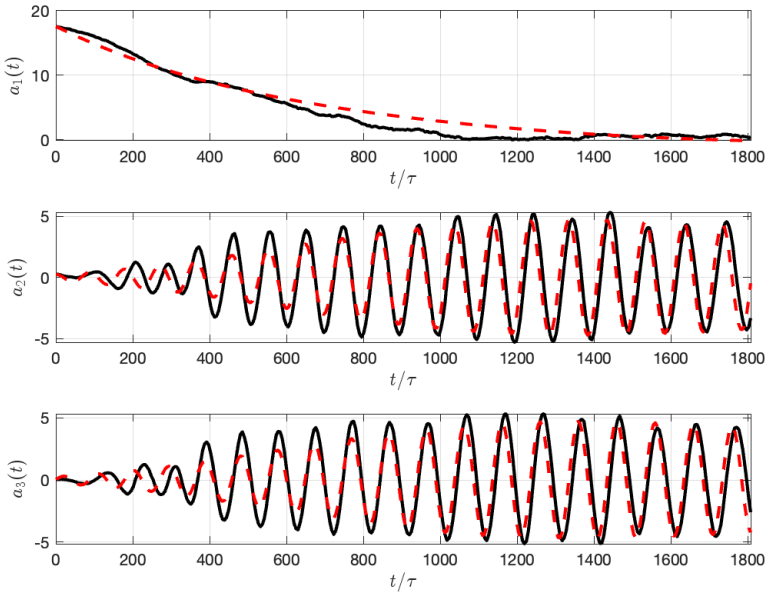

Figure 4.27: Comparison between ROM amplitude evolution (red dashed line) and real data (full black line)

5
Conclusions

The work addresses the formation of laminar separation bubbles. The scenario investigated involves varying environmental disturbances, which have received less attention in the literature than steady conditions. Despite the limited amount of work, cases involving varying disturbances are very common in practical situations [21]. Thus, the objective of this work is to develop and evaluate a physically interpretable reduced-order model that describes the formation of an LSB under a varying level of background disturbances. Therefore, the ROM aims to model the LSB from its initial separation to its quasi-stationary state. The experimental data for this work are provided by Horna (2024) [63]. The ROM was obtained by combining Galerkin projection strategy and Proper Orthogonal Decomposition of the data. POD was selected because it minimizes the mean squared error between the original data and its reduced linear approximation, expressed in terms of an orthonormal basis. Consequently, it naturally satisfies the conditions required for constructing a ROM via Galerkin projections. The final step of the methodology employed here is to determine the linear and bilinear coefficients of the Galerkin model. To this end, we used a Sparse Identification of Nonlinear Dynamics method. SINDy combines sparsity-promoting techniques with machine learning to infer governing equations from noisy measurement data for nonlinear dynamical systems.

POD decomposition of the velocity fields show that the first 15 modes contains more than 41% of the flow energy. Therefore, these modes were investigated. Among these 15 modes, the first four were the most energetic and so they were selected to build the ROM. In addition, the POD analysis indicated that the system evolved from one unstable steady state to another, then to a limit cycle. The vorticity transport equation of the Navier-Stokes equations was used to determine the instants at which these two steady-state solutions occur. According to this analysis, it was found that the candidate ROM needs to include at least four modes to capture the LSB dynamics. Thus, a model with these 4 modes was tested and analyzed.

The ROM accurately reproduces the system's trajectory on the underlying manifold, capturing the predominant dynamical features of the flow in

both the transient and quasi-steady regimes. The first and second mode growth rates and amplitudes in the limit cycle are correctly captured. These modes represent slow-varying disturbances associated with base-flow changes. The oscillatory modes show excellent agreement with the reference data in both growth rate and frequency.

An examination of the model coefficients reveals several interesting features. First, all four modes are linearly unstable. The model indicates that modes 1 and 2 are non-oscillatory (static) modes. In contrast, modes 3 and 4 together constitute a single complex oscillatory mode, characterized by the complex amplitude $A = a_3 + ia_4 \in \mathbb{C}$. The two static modes have linear growth rates approximately five times those of the oscillatory mode. Modes 1 and 2 are self-saturating, as evidenced by the negative sign of the quadratic self-interaction terms in Equations (4-7)–(4-8). The complex oscillatory mode is nonlinearly saturated by mode 1, while it amplifies mode 2. The squared modulus $|A|^2$ of the oscillatory amplitude enhances the effective linear instability of mode 1 and, conversely, saturates that of mode 2. Furthermore, mode 1 saturates the linear instability of mode 2, whereas mode 2 amplifies that of mode 1.

The ROM provides physical insights about the relation between modes. It is challenging to attribute a more specific physical meaning to the individual modes. To this end, it would be interesting to know their 3-D topology. In contrast, the oscillatory modes seem to be clearly associated with the K-H instability and vortex shedding dynamics. This last statement is consistent with the literature.

As evidenced by the POD analysis and the vorticity transport results, the dynamical system also evolves from an unstable point at a dimensionless time of approximately $time = 750$. To investigate this behavior, we proposed a model with only three modes to represent the late stages of bubble formation, almost at the onset of vortex shedding. To this end, we employed the same methodology as for the previous model. First, we recomputed the POD from the optimal time to the quasi-steady regime. The idea was to obtain the coherent structures and their corresponding temporal amplitude evolutions for a different base state. Based on the modal energy content and spatial characteristics, we selected the three most representative modes to describe the system dynamics. These modes were subsequently projected onto the governing equations to construct the POD-Galerkin model. The SINDy algorithm was then applied to identify the associated model coefficients.

The resulting reduced-order representation is consistent with the Landau equation, thereby providing strong evidence that a supercritical Hopf bifurca-

tion governs the system's dynamics. This, in turn, implies that the instability arises through a pair of oscillatory modes.

The model identifies a slaved *shift mode* and a pair of complex oscillatory modes, parametrized by the complex amplitude $A = a_3 + ia_4 \in \mathbb{C}$. This outcome is consistent with previous literature of ROMs for fluid flows. The growth rate of the slave mode is 4.7 times larger than that of the oscillatory mode, thereby ensuring the slave relationship between these modes. As anticipated, the ROM reproduces the essential dynamical features of the system. The first mode exhibit a smaller linear growth rate than observed in the reference data, which manifests as a slight delay in the linear growth of the oscillatory modes. Nevertheless, the ROM shows good agreement with the reference data.

In summary, the ROM proposed here was capable of reproducing well the system dynamics. The method's interpretability allows us to identify possible mechanisms for bubble formation. Thus, we consider that the main goals of the work were successfully achieved.

To ensure continuity of the present research, several directions can be pursued. First, the same framework can be employed to investigate supercritical laminar separation bubbles over a broader range of Reynolds numbers. Second, the model can be utilized to develop flow-control strategies informed by characteristic physical features of the LSB [37]. A more physics-oriented extension would be a detailed examination of the physical interpretation of the first and second modes of the four-degree-of-freedom model. Finally, model accuracy and/or physical insight may be enhanced through the application of machine learning and artificial intelligence techniques to automate the identification of state spaces, dominant modes, and underlying dynamical systems, for instance through shallow recurrent decoder networks [78]. Another possibility is the use of physics-informed neural networks for modeling the LSB.

Bibliography

[1] GASTER, M.. **The structure and behaviour of laminar separation bubbles**. ARC R&M, 1967.

[2] HORTON, H. P.. **Laminar separation bubbles in two and three dimensional incompressible flow.** PhD thesis, Queen Mary University of London, 1968.

[3] DIWAN, S. S.; RAMESH, O. N.. **Laminar separation bubbles: Dynamics and control**. Sadhana, 32(1):103–109, 2007.

[4] BENNY THOMPSON, E.; GUNASEKARAN, M.. **Review analysis on laminar separation bubble at low reynolds numbers**. Journal of Physics: Conference Series, 2054(1):012005, oct 2021.

[7] ALMUTAIRI, J.; ELJACK, E. ; ALQADI, I.. **Dynamics of laminar separation bubble over naca-0012 airfoil near stall conditions**. Aerospace Science and Technology, 68:193–203, 2017.

[8] LENGANI, D.; SIMONI, D.; UBALDI, M.; ZUNINO, P. ; BERTINI, F.. **Analysis of the reynolds stress component production in a laminar separation bubble**. International Journal of Heat and Fluid Flow, 64:112–119, 2017.

[9] DELLACASAGRANDE, M.; LENGANI, D.; SIMONI, D. ; YARUSEVYCH, S.. **A data-driven analysis of short and long laminar separation bubbles**. Journal of Fluid Mechanics, 976:R3, 2023.

[10] DOVGAL, A.; KOZLOV, V. ; MICHALKE, A.. **Laminar boundary layer separation: instability and associated phenomena**. Progress in Aerospace Sciences, 30(1):61–94, 1994.

[11] DUCOIN, A.; LOISEAU, J.-C. ; ROBINET, J.-C.. **Numerical investigation of the interaction between laminar to turbulent transition and the wake of an airfoil**. European Journal of Mechanics - B/Fluids, 57:231–248, 2016.

[12] ELJACK, E. M.. **The structure and dynamics of the laminar separation bubble**. Journal of Fluid Mechanics, 998:A56, 2024.

[14] GUNGOR, A. G.; SIMENS, M. P. ; JIMÉNEZ, J.. **Direct numerical simulations of wake-perturbed separated boundary layers**. Journal of Turbomachinery, 134(6):061024, 09 2012.

[15] LENGANI, D.; SIMONI, D.; UBALDI, M. ; ZUNINO, P.. **Pod analysis of the unsteady behavior of a laminar separation bubble**. Experimental thermal and fluid science, 58:70–79, 2014.

[16] SERNA, J.; LÁZARO, B.. **On the laminar region and the initial stages of transition in transitional separation bubbles**. European Journal of Mechanics-B/Fluids, 49:171–183, 2015.

[17] SERNA, J.; LÁZARO, B.. **On the bursting condition for transitional separation bubbles**. Aerospace Science and Technology, 44:43–50, 2015.

[19] MICHELIS, T.; YARUSEVYCH, S. ; KOTSONIS, M.. **Response of a laminar separation bubble to impulsive forcing**. Journal of Fluid Mechanics, 820:633–666, 2017.

[20] KURELEK, J. W.; KOTSONIS, M. ; YARUSEVYCH, S.. **Transition in a separation bubble under tonal and broadband acoustic excitation**. Journal of Fluid Mechanics, 853:1–36, 2018.

[21] YARUSEVYCH, S.; KOTSONIS, M.. **Steady and transient response of a laminar separation bubble to controlled disturbances**. Journal of Fluid Mechanics, 813:955–990, 2017.

[22] BRUNTON, S. L.; PROCTOR, J. L. ; KUTZ, J. N.. **Discovering governing equations from data by sparse identification of nonlinear dynamical systems**. Proceedings of the national academy of sciences, 113(15):3932–3937, 2016.

[23] CHAMPION, K.; ZHENG, P.; ARAVKIN, A. Y.; BRUNTON, S. L. ; KUTZ, J. N.. **A unified sparse optimization framework to learn parsimonious physics-informed models from data**. IEEE Access, 8:169259–169271, 2020.

[24] DE SILVA, B. M.; CHAMPION, K.; QUADE, M.; LOISEAU, J.-C.; KUTZ, J. N. ; BRUNTON, S. L.. **Pysindy a python package for the sparse identification of nonlinear dynamics from data**. arXiv preprint arXiv:2004.08424, 2020.

[25] ZHENG, P.; ASKHAM, T.; BRUNTON, S. L.; KUTZ, J. N. ; ARAVKIN, A. Y.. **A unified framework for sparse relaxed regularized regression: Sr3**. IEEE Access, 7:1404–1423, 2019.

[26] FOSTER, J.; DECUYPER, J.; DE TROYER, T. ; RUNACRES, M.. **Estimating a sparse nonlinear dynamical model of the flow around an oscillating cylinder in a fluid flow using sindy**. In: CONFERENCE ON NOISE AND VIBRATION ENGINEERING ISMA 2022, p. tba. ISMA 2022, Sept. 2022.

[27] TOPPINGS, C. E.; YARUSEVYCH, S.. **Laminar separation bubble formation and bursting on a finite wing**. Journal of Fluid Mechanics, 986:A26, 2024.

[28] TOPPINGS, C. E.; YARUSEVYCH, S.. **Transient dynamics of stall and reattachment at low reynolds number**. Journal of Fluid Mechanics, 1011:A38, 2025.

[29] RIST, U.; AUGUSTIN, K.. **Control of laminar separation bubbles**. Von Kármán Institute Lecture Series, 2003.

[30] KLOSE, B. F.; SPEDDING, G. ; JACOBS, G. B.. **Flow separation, instability and transition to turbulence on a cambered airfoil at reynolds number 20 000**. Journal of Fluid Mechanics, 1009:A9, 2025.

[31] MALMIR, F.; DI LABBIO, G.; LE FLOC'H, A.; DUFRESNE, L.; WEISS, J. ; VÉTEL, J.. **Low-frequency unsteadiness in laminar separation bubbles**. Journal of Fluid Mechanics, 999:A99, 2024.

[32] NOACK, B. R.; AFANASIEV, K.; MORZYŃSKI, M.; TADMOR, G. ; THIELE, F.. **A hierarchy of low-dimensional models for the transient and post-transient cylinder wake**. Journal of Fluid Mechanics, 497:335–363, 2003.

[33] NOACK, B. R.; TADMOR, G. ; MORZYNSKI, M.. **Actuation models and dissipative control in empirical galerkin models of fluid flows**. 6:5722–5727, 2004.

[34] COUPLET, M.; BASDEVANT, C. ; SAGAUT, P.. **Calibrated reduced-order pod-galerkin system for fluid flow modelling**. Journal of Computational Physics, 207(1):192–220, 2005.

[35] DENG, N.; NOACK, B. R.; MORZYŃSKI, M. ; PASTUR, L. R.. **Low-order model for successive bifurcations of the fluidic pinball**. Journal of fluid mechanics, 884:A37, 2020.

[36] LUCHTENBURG, D. M.; GÜNTHER, B.; NOACK, B. R.; KING, R. ; TADMOR, G.. **A generalized mean-field model of the natural and**

high-frequency actuated flow around a high-lift configuration. Journal of Fluid Mechanics, 623:283–316, 2009.

[37] TADMOR, G.; LEHMANN, O.; NOACK, B. R. ; MORZYŃSKI, M.. **Galerkin models enhancements for flow control**. In: REDUCED-ORDER MODELLING FOR FLOW CONTROL, p. 151–252. Springer, 2011.

[38] SCHLEGEL, M.; NOACK, B. R.. **On long-term boundedness of galerkin models**. Journal of Fluid Mechanics, 765:325–352, 2015.

[39] LOISEAU, J.-C.; BRUNTON, S. L.. **Constrained sparse galerkin regression**. Journal of Fluid Mechanics, 838:42–67, 2018.

[40] KERSCHEN, G.; GOLINVAL, J.-C.; VAKAKIS, A. F. ; BERGMAN, L. A.. **The method of proper orthogonal decomposition for dynamical characterization and order reduction of mechanical systems: an overview**. Nonlinear dynamics, 41(1):147–169, 2005.

[41] FLETCHER, C. A.. **Computational galerkin methods**. In: COMPUTATIONAL GALERKIN METHODS, p. 72–85. Springer, 1984.

[42] REMPFER, D.; FASEL, H. F.. **Dynamics of three-dimensional coherent structures in a flat-plate boundary layer**. Journal of Fluid Mechanics, 275:257–283, 1994.

[43] HIJAZI, S.; STABILE, G.; MOLA, A. ; ROZZA, G.. **Data-driven pod-galerkin reduced order model for turbulent flows**. Journal of Computational Physics, 416:109513, 2020.

[44] GIRFOGLIO, M.; QUAINI, A. ; ROZZA, G.. **A pod-galerkin reduced order model for the navier–stokes equations in stream function-vorticity formulation**. Computers & Fluids, 244:105536, 2022.

[45] SIROVICH, L.. **Turbulence and the dynamics of coherent structures. i. coherent structures**. Quarterly of applied mathematics, 45(3):561–571, 1987.

[46] LUMLEY, J. L.. **The structure of inhomogeneous turbulent flows**. Atmospheric turbulence and radio wave propagation, p. 166–178, 1967.

[47] HODSON, H. P.; HOWELL, R. J.. **Bladerow interactions, transition, and high-lift aerofoils in low-pressure turbines**. Annu. Rev. Fluid Mech., 37(1):71–98, 2005.

[48] TANI, I.. **Low-speed flows involving bubble separations**. Progress in Aerospace Sciences, 5:70–103, 1964.

[51] MARXEN, O.; HENNINGSON, D. S.. **The effect of small-amplitude convective disturbances on the size and bursting of a laminar separation bubble**. Journal of Fluid Mechanics, 671:1–33, 2011.

[52] MARXEN, O.; LANG, M. ; RIST, U.. **Vortex formation and vortex breakup in a laminar separation bubble**. Journal of Fluid Mechanics, 728:58–90, 2013.

[53] AVANCI, M. P.; RODRÍGUEZ, D. ; ALVES, L. S. D. B.. **A geometrical criterion for absolute instability in separated boundary layers**. Physics of Fluids, 31(1), 2019.

[55] REMPFER, D.. **Low-dimensional modeling and numerical simulation of transition in simple shear flows**. Annual review of fluid mechanics, 35(1):229–265, 2003.

[56] BERKOOZ, G.; HOLMES, P. ; LUMLEY, J. L.. **The proper orthogonal decomposition in the analysis of turbulent flows**. Annual review of fluid mechanics, 25(1):539–575, 1993.

[60] MANNEVILLE, P.. **Instabilities, chaos and turbulence**, volumen 1. World Scientific, 2010.

[61] BRUNTON, S. L.; NOACK, B. R.. **Closed-loop turbulence control: Progress and challenges**. Applied Mechanics Reviews, 67(5):050801, 2015.

[62] ROWLEY, C. W.; DAWSON, S. T.. **Model reduction for flow analysis and control**. Annual Review of Fluid Mechanics, 49(1):387–417, 2017.

[63] OMAR E. HORNA. **On the formation of a laminar separation bubble in a two dimensional boundary layer**. Ph.d. thesis, Pontifical Catholic University of Rio de Janeiro, 2024.

[64] LIAO, Z.-M.; ZHAO, Z.; CHEN, L.-B.; WAN, Z.-H.; LIU, N.-S. ; LU, X.-Y.. **Reduced-order variational mode decomposition to reveal transient and non-stationary dynamics in fluid flows**. Journal of Fluid Mechanics, 966:A7, 2023.

[65] LANG, M.; RIST, U. ; WAGNER, S.. **Investigations on controlled transition development in a laminar separation bubble by means of LDA and PIV**. Experiments in Fluids, 36(1):43–52, 2004.

[66] MAYLE, R. E.. **The role of laminar-turbulent transition in gas turbine engines**. In: TURBO EXPO: POWER FOR LAND, SEA, AND AIR, volumen 79023, p. V005T17A001. American Society of Mechanical Engineers, 1991.

[67] MITRA, A.; RAMESH, O.. **New correlation for the prediction of bursting of a laminar separation bubble**. AIAA Journal, 57(4):1400–1408, 2019.

[69] SIMONI, D.; UBALDI, M.; ZUNINO, P.; LENGANI, D. ; BERTINI, F.. **An experimental investigation of the separated-flow transition under high-lift turbine blade pressure gradients**. Flow, turbulence and combustion, 88(1):45–62, 2012.

[70] RODRÍGUEZ, D.; THEOFILIS, V.. **Structural changes of laminar separation bubbles induced by global linear instability**. Journal of Fluid Mechanics, 655:280–305, 2010.

[71] PANISSET, P. B. P.; PINEDO, O. E. H. ; DE PAULA, I. B.. **Investigation of transient regime in laminar separation bubble**. Advances in Turbulence: Selected Papers from the XII Spring School on Transition and Turbulence, p. 121, 2023.

[72] WAHIDI, R.. **An experimental investigation of airfoils with laminar separation bubbles and effects of distributed suction**. Mississippi State University, 2009.

[73] RODRÍGUEZ, D.; GENNARO, E. M. ; JUNIPER, M. P.. **The two classes of primary modal instability in laminar separation bubbles**. Journal of Fluid Mechanics, 734:R4, 2013.

[74] RAFFEL, M.; WILLERT, C. E.; SCARANO, F.; KÄHLER, C. J.; WERELEY, S. T. ; KOMPENHANS, J.. **Particle image velocimetry: a practical guide**. Springer, 2018.

[75] CAVALIERI, A. V.; NOGUEIRA, P. A.. **Reduced-order galerkin models of plane couette flow**. Physical Review Fluids, 7(10):L102601, 2022.

[76] CAVALIERI, A. V.. **Structure interactions in a reduced-order model for wall-bounded turbulence**. Physical Review Fluids, 6(3):034610, 2021.

[77] MAIA, I. A.; CAVALIERI, A.. **Turbulence suppression in plane couette flow using reduced-order models**. Journal of Fluid Mechanics, 1014:A18, 2025.

[78] WILLIAMS, J. P.; ZAHN, O. ; KUTZ, J. N.. **Sensing with shallow recurrent decoder networks**. Proceedings of the Royal Society A, 480(2298):20240054, 2024.

A
Four degree of freedom derivation

The reduced-order mathematical representation characterizing a supercritical Hopf bifurcation can be expressed as follows:

$$\dot{a}_1 = \sigma_1 a_1 + \beta_1(a_2^2 + a_3^2)$$

$$\dot{a}_2 = \sigma a_2 - \omega a_3, \qquad \sigma = \sigma_2 + \beta_2 a_1$$

$$\dot{a}_3 = \omega a_2 + \sigma a_3, \qquad \omega = \omega_2 + \gamma_2 a_1$$

The temporal evolution of the *shift mode* is described by $\dot{a}_3$. This mode can be represented by two basis modes, denoted by e_1 and e_2, whose linear relation is given by $e_1 - e_2$. Substituting this expression into equation Hopf, we obtain:

$$\dot{e}_1 - \dot{e}_2 = \sigma_1(e_1 - e_2) + \beta_1(a_2^2 + a_3^2)$$

$$\dot{a}_2 = \sigma a_2 - \omega a_3, \qquad \sigma = \sigma_2 + \beta_2(e_1 - e_2)$$

$$\dot{a}_3 = \omega a_2 + \sigma a_3, \qquad \omega = \omega_2 + \gamma_2(e_1 - e_2)$$

Since $a_1^2 \cong a_2^2 + a_3^2$, the term $a_1^2 \cong (e_1 - e_2)^2$ can likewise be interpreted as an additional degree of freedom. Consequently, it was incorporated into the model, yielding:

$$\dot{e}_1 - \dot{e}_2 = \sigma_1(e_1 - e_2) + \beta_1(a_2^2 + a_3^2) + \gamma_1(e_1 - e_2)^2$$

$$\dot{a}_2 = \sigma a_2 - \omega a_3, \qquad \sigma = \sigma_2 + \beta_2(e_1 - e_2)$$

$$\dot{a}_3 = \omega a_2 + \sigma a_3, \qquad \omega = \omega_2 + \gamma_2(e_1 - e_2)$$

The resulting system of equations, obtained after full expansion and simplification, is given by:

$$\dot{e}_1 + (-\dot{e}_2) = [-\sigma_1 e_1 - \gamma e_1 e_2 + \gamma_1 e_1^2] + [\sigma_1 e_2 - \gamma_1 e_1 e_2 + \gamma_1 e_2^2] + \beta_1(a_2^2 + a_3^2)$$

$$\dot{a}_2 = \sigma a_2 - \omega a_3, \qquad \sigma = \sigma_2 + \beta_2(e_1 - e_2)$$

$$\dot{a}_3 = \omega a_2 + \sigma a_3, \qquad \omega = \omega_2 + \gamma_2(e_1 - e_2)$$

By decomposing the first equation into two separate expressions, where e_1 denotes the temporal evolution of the first POD mode amplitude and e_2 denotes the temporal evolution of the second POD mode amplitude, and by relaxing the initially assumed symmetry constraints, the system attains its final mathematical form.

The hypothesis of symmetry breaking is justified by the fact that the modes do not describe identical dynamical behavior; consequently, the associated coefficients cannot be assumed to be symmetric.

$$\dot{a}_1 = \sigma_1 a_1 - \zeta_1 a_1 a_2 + \beta_1(a_3^2 + a_4^2) - \gamma_1 a_1^2$$

$$\dot{a}_2 = \sigma_2 a_2 - \zeta_2 a_1 a_2 - \beta_2(a_3^2 + a_4^2) - \gamma_2 a_2^2$$

$$\dot{a}_3 = \sigma a_3 - \omega a_4, \qquad \sigma = \sigma_3 - \beta_3 a_1 + \beta_4 a_2$$

$$\dot{a}_4 = \omega a_3 + \sigma a_4, \qquad \omega = \omega_3 - \gamma_3 a_1 - \gamma_4 a_2$$